Title
ACTINIDE PRODUCTION FROM XENON BOMBARDMENTS OF CURIUM-248

Author
Welch, R.B.

Publication Date
1985

Lawrence Berkeley Laboratory
UNIVERSITY OF CALIFORNIA

ACTINIDE PRODUCTION FROM XENON BOMBARDMENTS OF CURIUM-248

R.B. Welch
(Ph.D. Thesis)

January 1985

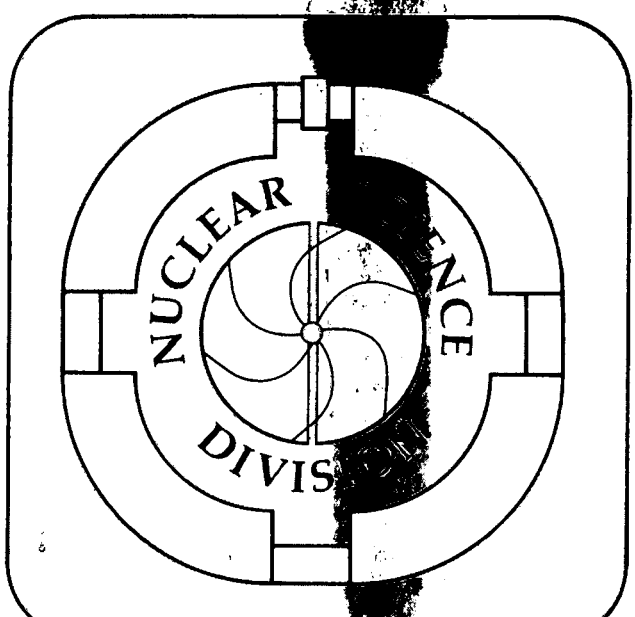

Prepared for the U.S. Department of Energy under Contract DE-AC03-76SF00098

DISCLAIMER

LBL-19010

ACTINIDE PRODUCTION FROM XENON BOMBARDMENTS OF CURIUM-248

Robert B. Welch

Ph.D. Thesis

January 1985

Department of Chemistry
Lawrence Berkeley Laboratory
University of California
Berkeley, CA 94720

This work was supported by the Director, Office of Energy Reasearch, Division of Nuclear Physics of the Office of High Energy and Nuclear Physics of the U.S. Department of Energy under Contract DE-AC03-76SF00098.

Actinide Production from Xenon Bombardments of Curium-248

Robert B. Welch

ABSTRACT

Production cross sections for many actinide nuclides formed in the reaction of ^{129}Xe and ^{132}Xe with ^{248}Cm at bombarding energies slightly above the coulomb barrier were determined using radiochemical techniques to isolate these products. These results are compared with cross sections from a ^{136}Xe + ^{248}Cm reaction at a similar energy. When compared to the reaction with ^{136}Xe, the maxima in the production cross section distributions from the more neutron deficient projectiles are shifted to smaller mass numbers, and the total cross section increases for the production of elements with atomic numbers greater than that of the target, and decreases for lighter elements. These results can be explained by use of a potential energy surface (PES) which illustrates the effect of the available energy on the transfer of nucleons and describes the evolution of the di-nuclear complex, an essential feature of deep-inelastic reactions (DIR), during the interaction. The other principal reaction mechanism is the quasi-elastic transfer (QE). Analysis of data from a similar set of reactions, Xe-

129, 132, and 136 with Au-197, aids in explaining the features of the Xe + Cm product distributions, which are additionally affected by the depletion of actinide product yields due to deexcitation by fission. The PES is shown to be a useful tool to predict the general features of product distributions from heavy ion reactions.

January 11, 1985

Acknowledgments

Many people and institutions have been invaluably helpful in getting me this far, and I would like to thank a few of them here.

The University of California admitted me into the graduate program in chemistry at Berkeley.

Glenn T. Seaborg let me join his research group, the SHEIKS, and provided the necessary guidance.

All the SHEIKS, past and present, graduate and undergraduate, foreign and domestic, created a fun and productive work environment. Special thanks are in order to Ken Moody, Ken Gregorich and Diana Lee, who did so much of the chemical work for this work.

The staff and crew of the SuperHILAC were essential, because I could not have done the experiments without them.

Don Reents always seemed to be there to help out during a crisis.

The Chemistry Department at Drake University was influential in my choice to pursue a degree in chemistry instead of some other science.

Comics & Comix and Silverball Gardens provided alternate realities to the People's Republic of Berkeley..

Ayn Rand showed me the vision of a rational world.

I wish to express my appreciation to all of my friends in the Bay Area, Des Moines and throughout the world who have stuck by me and helped me learn a bit about the real world during these last few years. I hope to return the favor someday.

Most importantly, I thank my family for the endless support I have received. They were always there (via AT&T or in person), during my bitterest defeats, my loneliest moments, and my too infrequent triumphs. Dad, Mom, Dale, Jean and

Ted : I couldn't have done it without you.

This work was supported by the Director, Office of Energy Research, Division of Nuclear Physics of the Office of High Energy and Nuclear Physics of the U.S. Department of Energy under Contract DE-AC03-76SF00098.

Table of Contents

Actinide Production from Xenon Bombardments of Curium-248

Robert B. Welch

1. Purpose and Introduction

The purpose of this work is to study the effect on actinide nuclide production by use of the more neutron deficient, non-closed shell projectiles xenon-129 and xenon-132 as compared with xenon-136. The differences observed can be explained with the use of potential energy surfaces, which describe the relative energy differences between the possible products from a given reaction. We can also get an insight into the reaction mechanisms involved in these low energy heavy ion reactions.

The complexity of a projectile-induced nuclear reaction is roughly proportional to the total mass involved. A proton or alpha particle bombarding a relatively light target, such as iron, can either knock out some other light particles or can be absorbed, creating a compound nucleus, which then deexcites by emitting mainly gamma rays and neutrons. On the other hand, a heavy ion such as xenon bombarding curium can cause many different products to be formed. Grazing collisions can lead to transfer of a few nucleons from projectile to target or vice versa. More central collisions can lead to a deep inelastic collision, a two body interaction which can lead to large net nucleon transfers. The target-like product is formed in an excited state and can deexcite by neutron emission or by fission. Thus, there are many possible products from a heavy ion-heavy target

interaction. Because of the possibility of large net nucleon transfers to the target nuclei, heavy ion bombardments of actinide targets are a means to make nuclides that cannot be made by other methods, such as successive neutron capture in nuclear reactors. A study of how much of each product is formed is helpful in explaining the mechanism involved.

Previous work done in the field of heavy ion bombardments of actinide targets by our group (or in collaboration with others) has involved the use of projectiles such as ^{136}Xe, ^{86}Kr [Moo83], and ^{48}Ca [Gäg83], all of which are the most neutron-rich isotopes of their respective elements. As one goes to heavier elements, one needs a larger neutron-to-proton ratio to have a nucleus that is stable to beta decay. The longest lived isotopes of the heaviest elements are expected to be beta stable and have an odd mass number, which increases the partial half-life for decay by spontaneous fission of that nuclide. Also, new neutron-rich isotopes of previously known elements will be made best by use of neutron-rich projectiles. Another common property of ^{136}Xe, ^{86}Kr, and ^{48}Ca is that they all have a closed neutron shell configuration. Shell model theory states that there are certain "magic" numbers of neutrons or protons that have an additional stability. These magic nuclides have, for example, larger binding energies and lower alpha decay energies than can be predicted from use of the liquid drop model of the nucleus. To determine the effect of non-closed shell and more neutron deficient projectiles on the production cross-sections of actinide nuclides formed in heavy ion reactions, we bombarded ^{248}Cm with ^{129}Xe and ^{132}Xe and compared actinide production cross sections from these reactions with those from ^{136}Xe with ^{248}Cm (at similar energies on target) [Moo83].

2. Heavy Ion Reactions - Theory

Heavy ion interactions can involve a number of reaction mechanisms. If the projectile has enough energy to overcome the mutual coulomb repulsion between it and the target nucleus, the angular momentum of the system plays a major role in determining which mechanism is to be followed. Large angular momenta correspond to large impact parameters and grazing collisions, where the two nuclei only slightly overlap. The nuclear strong force is not strong enough to hold the reactants together for long, and so they have time to exchange or knock out only a few nucleons before they separate. These reactions are called quasi-elastic reactions (QE) because there is little change, if any, in the kinetic energy or mass of the projectile. At smaller angular momenta, there is greater overlap, resulting in longer interaction times. During the contact time, the two participants form a di-nuclear complex, but do not completely fuse. This is the domain of the deep inelastic reaction (DIR). There is an exchange and transfer of many nucleons back and forth as the di-nuclear complex slowly rotates. Nucleon exchange appears to be the primary kinetic energy loss mechanism. Eventually, the angular momentum of the rotating system causes it to break apart into a target-like product and a projectile-like product. Most of the initial kinetic energy of the projectile is converted into excitation energy of the products and so they often separate from each other with kinetic energies as low as that amount attributable to their mutual coulomb repulsion. This is the inelastic part of DIR. For very large systems (those with total mass number $A > 250$), QE and DIR are the only significant mechanisms involved [Gob81]. Nearly head-on collisions would lead to complete fusion in the case of lighter projectiles. However, fusion has not been found to occur for projectiles heavier than Zr on heavier targets [Arm82].

The characteristics of a QE reaction are 1.) sharply peaked narrow mass

distributions centered around the projectile and target masses, 2) little energy loss and little angular momentum transfer to the products, 3) a narrow angular distribution of projectile-like products peaked slightly forward of the grazing angle in the center of mass frame (c.m.), while target-like products recoil in the opposite direction in c.m. For a DIR, one sees 1) a broad double humped mass distribution centered near, but not necessarily at, the projectile and target masses, 2) much kinetic energy damping, reappearing as excitation energy of products, 3) large angular momentum transfer between products and 4) very broad angular distribution centered in c.m. frame near the grazing angle and its supplement for the system. Near-target nuclides are made principally by QE, although DIR will contribute some. Nuclides which involve a larger transfer - more than about 6 nucleons - are formed primarily by DIR. Because of the two body nature of DIR and QE, the same production properties apply to projectile-like products. However, in this work, only target-like products were studied. For a more extensive review of deep inelastic reactions, refer to [Mor83], [Vol78] and [Sch77].

Much work has been done to determine what governs the final distributions of mass, energy, and angular momentum during a DIR. The most probable excitation energy distribution is proportional to the mass of the product. However, there is a width to the distribution which allows a small probability of a product being formed in a relatively cold state. The transfer of angular momentum depends on how the nuclei move in relation to one another during contact. The 2 reactants could rotate as one or could roll independently as they stick together. The intrinsic angular momentum of the transferred nucleons is also important.

The net movement of nucleons appears to depend on the system's effort to equilibrate various modes, such as the neutron-to-proton (N/Z) ratio and the mass asymmetry. Mass asymmetry controls whether the system tries to make 2

products of equal mass or tries to fuse the reactants into one product. The N/Z mode causes a rapid rearrangement of protons and neutrons between the reactants without a significant net mass change in either participant. The equilibrium N/Z value of the products is determined by the interplay of the coulomb, centrifugal and nuclear potentials, as well as by the masses of the products, and can be roughly approximated by the N/Z ratio of the combined system. The N/Z mode equilibration time is about 10^{-22} seconds [Kra77], while attainment of mass asymmetry takes about 10^{-20} seconds. Even after equilibration, statistical fluctuations in nucleon movement cause a distribution in product masses which is peaked at the equilibrated value. Thus, there is a small, finite probability of a very neutron (or proton) -rich product being made. Because of the fluctuations in excitation energy and number of nucleons, DIR may be the best and only way to produce some neutron-rich actinide nuclides.

The life time of the dinuclear complex depends on the amount of overlap of the participants due to the impact parameter of the given collision. The total kinetic energy loss (TKEL), which is the difference in kinetic energy between the reactants and products, is a good measure of the interaction time because the TKEL monotonically increases as a function of the interaction time. Determination of the evolution of product distributions as a function of TKEL has proved helpful in interpreting and explaining DIRs.

When using a more neutron deficient isotope as a projectile, it is expected that the peaks of the elemental cross sections should shift to lighter (i.e. more neutron deficient) nuclides. This shift is expected for DIR products because the equilibrated N/Z value is smaller due to the neutron-poor projectile, causing an overall movement of neutrons from the target to the projectile. Because there are fewer neutrons in Xe-129 than in Xe-136, there is a smaller probability of transferring a neutron in a QE interaction, and so neutron-rich products are less

likely to be made.

3. Bombardments

Production cross-sections were determined for actinide products formed in three bombardments of a ^{248}Cm target. The curium target used contained 0.485 mg/cm^2 ^{248}Cm, electroplated as the oxide on a 0.5 mil beryllium backing. The curium in the target is 97.4% ^{248}Cm in isotopic composition, along with 2.6% ^{246}Cm and $1x10^{-4}$% ^{244}Cm. The target was made by electroplating layers of curium nitrate from an isopropanol solution and converting them to the oxide form by heating to 300° C [Mul75,Moo83]. The thickness of the target was determined by counting the alpha radiation of the curium with a surface barrier detector and a multichannel analyzer.

The xenon ions were supplied and accelerated by Lawrence Berkeley Laboratory's Super-Heavy Ion Linear ACcelerator(SuperHILAC), an Alvarez- type linear accelerator capable of accelerating ions as heavy as ^{238}U to an energy of 8.5 MeV/nucleon with intensities of nearly 1 particle microampere [SHL76]. The prestripper section of the accelerator accepts ions with energies of 113 keV/nucleon and accelerates them to 1.2 MeV/nucleon. After passing through thin carbon stripper foils to increase the charge on the ions, the post-stripper section accelerates them to the maximum of 8.5 MeV/nucleon. Lower final energies can be obtained by turning off the radiofrequency field in the later tanks in the post-stripper or by adjusting the gradient of the radio frequency field in the last tank used. The SuperHILAC has 3 injectors and with computer control is able to deliver 3 different ions as part of the 36 pulse per second beam. The newest injector, Abel, was designed to give higher intensity heavy ion (A>86) beams than can be delivered by the other injectors [Sta81]. Abel consists of a combination Cockroft-Walton (CW) preaccelerator, which contains the ion source, and a Widerõe accelerator, which accelerates the ions to 113 keV/nucleon, the energy needed by the prestripper of the SuperHILAC. A charge stripper utilizing

Fomblin vapors (high molecular weight linear chain fluorocarbons) is situated between the Wideröe and the SuperHILAC. The transport line in Abel has a right angle bend between the CW and the Wideröe, allowing the selection and acceleration of one isotope from a natural source. Natural xenon, which consists of 26.4% ^{129}Xe and 27% ^{132}Xe among its 9 stable isotopes, was used as the source in these experiments. After reaching the desired energy, the ions leave the SuperHILAC and travel down the beamline to S-cave, the location of the target system. Because there are no bending magnets between the exit of the SuperHILAC and S-cave, it is necessary to do extra tuning on the beam to ensure that no ions from other beams concurrently accelerated come through to S-cave. The beam integral is determined by integrating the current that passes through the target, and extraneous ions from other beams will cause an erroneously high beam integral to be recorded. Also, the unwanted ions may have high enough energy to react with the target nuclei, yielding products which we would assume were formed by the interaction of the correct ion with the target. During the bombardment, the ions react with the target nuclei and the products recoil out of the target and stop in a catcher foil. Chemical separation of the product atoms from the catcher foil and the measurement of the decay energies and half lives of the radioactive products found determine how much of each product was made.

After entering S-cave, the ions pass through a 60 cm diameter scattering chamber and enter the target system. Figure 3.1 is an exploded view of the target system. The beam passes through a water cooled 6 mm graphite collimator. The target is cooled by nitrogen gas, and a Havar window separates the nitrogen from the vacuum of the SuperHILAC. Havar is a strong alloy of 9 metals, the most abundant being cobalt, chromium, iron, and nickel. After passing through the target, unreacted beam is stopped by a water cooled beam stop. The catcher foil holder is between the target and beam stop. The catcher foils are shaped like truncated cones and stop the products which recoil out of the target at an angle

of 20-60 degrees from the beam. If desired, the more forward recoiling products can be stopped in a separate catcher placed against the beam stop. However, products from beam ions reacting with catcher material would also be in an end piece catcher, and chemical purity of the sample to be counted becomes critical because of relatively small amounts of actinide product nuclei compared to other products. Because some actinide products have short half lives, the target system is designed to allow rapid access to the target and the catcher foil. Since one need only close a valve and bring the target system up to atmospheric pressure, it takes only 2 to 3 minutes from the end of bombardment to dismount the catcher foil and begin transporting it to the chemistry laboratory. The target system is also designed to handle highly radioactive targets (the curium target used decayed at a rate of about 10^6 dps). If the target should break and be sucked into the SuperHILAC, a major effort would be needed to decontaminate the accelerator. The potential for this catastrophe is eliminated by the presence of a quickly activated slammer valve situated just outside S-cave. If the pressure in the beam line should suddenly rise, which could be a indication of a target failure, a teflon wedge is explosively fired into the beamline and prevents upstream contamination. With a radioactive target, beam cannot be sent into S-cave unless the slammer valve is armed. Less catastrophic failures are prevented by an interlock system which turns off the beam if conditions occur which could lead to target damage. The collimator and end piece water pressure and temperature, nitrogen gas pressure, beam current, and an infrared meter are all connected to the interlock system.

The energy of the beam ions is appreciably degraded by their passage through the Havar window, nitrogen cooling gas and the beryllium backing. The range and stopping power tables of Hubert, et. al. [Hub80] were used to predict the energy loss through the various pieces of the target system. The computer program RANGY was developed to use the stopping power tables to interpolate

energy loss through compounds and other untabulated media [Moo80]. We determined that if the ions passed through the beryllium target backing before reaching the target, the beam energy on target would be above the coulomb barrier of the ion-target system only when the initial energy of the beam is nearly the maximum obtainable from the SuperHILAC. The largest energy loss occurs in low atomic number media such as beryllium. In order to get higher energies on the target, the beryllium would need to be thinner or else the target would have to be turned around so that the ions hit the target without being degraded by the beryllium. In the latter case, however, the product nuclei would have to recoil through the beryllium. Our calculations indicate that the energy of these products corresponds to a range nearly equal to that in the beryllium and therefore, some of them would not get out. We chose to run these experiments with the target facing the catcher foil to minimize loss of products in other media.

The energy of an ion accelerated by the SuperHILAC is determined by the SuperHILAC's own set of surface barrier detectors, which are located in various positions along the beam line from the SuperHILAC to the target system or by a phase probe measurement. The phase probe system measures the velocity of the ions by using the relative phases of the radiofrequency fields in the accelerating sections of the SuperHILAC. To determine the actual energy of the beam as it passed through successively more and more segments of the target system, we measured the energy with a specially modified target system endpiece which included a surface barrier detector.

For this work, 3 projectile-energy-target systems were studied:

1) ^{129}Xe(hi): 8.49 MeV/A from the SuperHILAC, 791 - 769 MeV on target, 1.09 B_c.

2) ^{129}Xe(lo): 7.89 MeV/A from the SuperHILAC, 723 - 700 MeV on target, 1.00 B_c.

3) ^{132}Xe: 8.47 MeV/A from the SuperHILAC, 817 - 793 MeV on target, 1.12 B_c.

where B_c is the Couloumb barrier between the nuclei. This barrier represents

the minimum kinetic energy needed bring the nuclei into contact. The separation distance used to calculate the barrier is:

$$R = 1.36 * (A_1^{1/3} + A_2^{1/3}) + .5 \quad \text{fm} \qquad (3.1)$$

where A_1 and A_2 are the mass numbers of the two nuclei.

The range in energies on target shows the energy loss of the projectiles as they pass through the target material. The Hubert stopping power tables accurately predict these energy losses and therefore could be used to determine the energy on target in some of the bombarding systems.

4. Chemical Procedures and Data Accumulation

At the end of the bombardments, the catcher foils, which contain the reaction products, were transported to the chemistry laboratory, where the desired chemical fractions were separated from other products and the catcher foil material. Chemical techniques for the identification of product nuclides have the advantage of high selectivity and isolation factors, along with Z identification of the products. Analysis of parent-daughter activities is simplified by knowing the chemical composition of a sample at the moment of chemical separation. The large chemical separation factors allow detection of small levels of activity corresponding to products with small production cross sections. The major disadvantage of chemical separation procedures is the time involved, which puts a lower limit on the half life of observed products.

During a given experiment, the length of a bombardment is coordinated with the half-lives of the particular radionuclides being investigated, and the chemical procedure used depends on the nuclear as well as chemical properties of the desired products. Short bombardments maximize the amounts of short-lived activities while limiting the production of longer lived activities. Also, sources of nuclides which decay by alpha emission must be thin enough not to degrade the energy and intensity of the alpha particles when being detected. Sources of nuclides which are detected by gamma-ray emission can be much thicker since gamma rays are much more penetrating than alpha rays.

The efficiency of a chemical separation procedure is determined by use of a radioactive tracer. A known activity of the tracer is added to the sample at the start of the procedure. The tracer undergoes the same chemical reactions as the product nuclei of the same element. The fraction of the activity of the tracer that appears in the final sample equals the fraction of desired product nuclei in the counted sample. The three general chemical procedures used for this

project are described next.

First, separate samples containing mainly short-lived Bk, Cf, Es, and Fm products were prepared following a 4 to 6 hour bombardment. The procedure is summarized in Figure 4.1. After dissolution of the gold catcher foil, actinide nuclides were separated from lanthanides by elution of the actinides with 13M HCl off of a cation exchange column [Tho54]. The solution containing the actinides was loaded next onto another cation exchange column and individual actinides were eluted with alpha- hydroxyisobutyric acid (HIBA) [Cho56]. The sources were thin enough to be counted for alpha activity as well as for gamma activity, and were ready for counting in about 1 hour after the end of the bombardment. No tracers were used, so no chemical yield was directly determined. However, comparison of relative production cross section of a nuclide with its experimentally determined cross section obtained by use of another procedure where tracers were used allows us to determine absolute cross sections for other nuclides observed in the tracerless experiments. This bombardment was used to determine cross sections for short-lived (half lives of 15 to 60 minutes) nuclides that would be unobservable in the long bombardment due to the latter's longer separation time (4 to 6 hours). The nuclides found only in this bombardment include ^{245,247}Cf, and ^{250}Es. We also looked for, but failed to find, ^{250}Fm.

The second chemical procedure was designed to quickly separate americium products. The cross sections for the neutron-rich isotopes Am-245, 246, 246m, and 247 are among the largest for any actinide product produced from a ^{248}Cm target because of the small nucleon transfer necessary to make such products. A quick separation is needed because all of these nuclides have half lives of less than 40 minutes, except for the 2.05 hour ^{245}Am. The overall procedure is adapted from [Moo63] and is based on the ability to oxidize the most common and stable americium ion in acidic solution, Am(III), to Am(VI) by use of the

powerful oxidizing agent ammonium peroxydisulfate $(NH_4)_2S_2O_8$. The procedure is outlined in Figure 4.2. The catcher foil for this procedure was aluminum, which rapidly dissolves in hot 10M NaOH. ^{241}Am was added as a tracer and the solution was diluted with water. After a small amount of La(III) carrier was added, a lanthanum hydroxide precipitate formed which carried with it the other +3 ions such as the lanthanides, actinides, and yttrium, but does not carry the aluminum, which stays in solution as $Al(OH)_4^-$. After washing the precipitate with 1M ammonium hydroxide, it was dissolved with 1M nitric acid. A freshly prepared solution of ammonium peroxydisulfate was added to the solution, along with a drop of Ag^+, which serves as a catalyst for the oxidation of the americium. After heating the solution for several minutes, excess fluoride ion is added to precipitate the lanthanum carrier, which should also carry all other +3 actinides and lanthanides, and other fluoride-insoluble ions. The Am(VI) does not coprecipitate with the LaF_3, probably because the fluoride ion forms a stable complex with the Am(VI). The LaF_3 precipitate is discarded and manganous nitrate is added to the supernatant solution to reduce the Am(VI) back to Am(III). Addition of lanthanum carrier leads to the precipitation of lanthanum fluoride with the coprecipitation of the Am(III) fluoride and the final source, the lanthanum fluoride precipitate, is counted for gamma activity. Other actinides, such as uranium, neptunium, plutonium and berkelium can be oxidized to high oxidation states and could follow Am through the chemistry. However, no gamma rays from other actinides have been observed in an americium sample. The cross sections for the production of neptunium and uranium are too small, and the half-lives of the neutron-rich plutonium isotopes are too long to cause enough activity to be detected. Berkelium would be easy to detect if present, since ^{250}Bk has a large production cross section, some intense gamma rays in its decay and a relatively short half-life (3.2 hr). It has not been detected in americium fractions probably because the +4 state is not as well stablized by fluoride

ion as is Am(VI) causing the Bk to coprecipitate with the first LaF_3 precipitate. Thus, only the desired americium products are observed. After all of the short lived Am activities had decayed away, the LaF_3 precipitate from the short Am chemistry from the bombardment with ^{132}Xe was dissolved with HNO_3-H_3BO_3. The actinide nuclides were separated from the lanthanum and other lanthanide nuclides by elution with saturated HCl on a cation exchange column. The resulting sample was counted for α activity due to ^{242}Cm which would be produced by β^- decay of ^{242g}Am.

The most important step in achieving large chemical yields is the oxidation of Am(III) to Am(VI). The fraction of americium that is oxidized increases with the length of time the solution sits after addition of the $S_2O_8^{-2}$. One must compromise between longer oxidation time and overall chemical separation time. Chemical yields averaged about 50 % when the separation time was reduced to 30 to 40 minutes.

The final chemical procedure is used to separate chemical fractions of all elements from uranium to fermium from a gold catcher foil after a long (ideally, at least 24 hours) bombardment. The procedure is described in detail in [Moo83], summarized in Figure 4.3, and a short review is provided here. The gold catcher foil is dissolved in aqua regia and loaded on an anion exchange column. The trans-plutonium actinides are eluted with 9M HCl, while the gold, uranium, neptunium and plutonium remain on the column. The U, Np, and Pu are stripped from the column with water, ferrous ion and a .1M HCl/1M HF solution. The ferrous ion slowly reduces the Au(III) to the metallic state in order to keep the Au(III) from complexing with the fluoride ions. Addition of lanthanum carrier causes the Np and Pu to coprecipitate with lanthanum fluoride, while the U stays in solution. The precipitate is dissolved with boric acid and loaded on an anion exchange column. The Pu is eluted with 1M HI/10M HCl and Np is removed with

4M HCl/.1M HF. The solution containing the U is made strongly basic, causing ferric hydroxide to precipitate. This is next dissolved with nitric acid and the U is extracted with diethyl ether. Each of the solutions containing U, Np, and Pu is evaporated to dryness on platinum disks to make sources for counting.

The transplutonium actinides are loaded onto a heated cation column and can be individually eluted in the order Fm-Es-Cf with pH 3.7, 0.5M HIBA. Am, Cm, and Bk are stripped from the column with pH 4.2 HIBA and loaded onto another cation column. Saturated hydrochloric acid is used to separate these actinides from any lanthanides still present and the resulting solution is evaporated and plated out on platinum, giving a combined Am-Cm-Bk source. These samples were ready for counting 4 to 6 hours after the end of bombardment.

Upon completion of the chemical separations, the fractions are placed in front of the appropriate detectors and the energy spectra of the radioactivities present are accumulated and stored. Alpha and spontaneous fissions activities are simultaneously detected by standard Si(Au) surface barrier detectors [Kno79]. Because of the limited range of alpha particles in air, the detectors are placed in chambers kept at a pressure of about 30 microns. Electrons produced by the interaction of the alpha particles or fission fragments with the silicon in the detector are separated from the corresponding holes and collected with an applied bias of 50 V. The charge collected is proportional to the energy deposited in the sensitive volume of the detector. The output voltage from the preamplifier is split and fed into 2 amplifiers. One signal is deciphered into an energy spectrum of the alpha particles, covering an energy range of 5-10 MeV. If the signal corresponds to an energy greater than 15 MeV, a single channel analyzer records the event as a fission. The detectors are calibrated for energy determination by use of ^{241}Am, ^{244}Cm, and ^{252}Cf standards. The ^{252}Cf source also supplies fission events. The efficiency of the detectors was determined by use of a ^{241}Am stan-

dard and found to be 22.4 ± 1.0% for alpha particles. The efficiency for the detection of fission fragments is assumed to be exactly twice as much. Care is taken to be sure that all sources sit directly over the center of the detector in order to maximize the detection efficiency of the sample. The detectors are on a computer controlled cycle of accumulation for a preset time, writing the spectrum to a magnetic tape, and then clearing the spectrum to allow accumulation of the next one. Background activities contribute very few events to an alpha particle spectrum, allowing identification of very low-level activities. The Cf, Es, and Fm fractions were all counted on this system, as was the ^{237}Np, ^{238}Pu and ^{241}Am tracers (used to determine Np, Pu, and Am chemical yields).

Gamma radiation from radioactive decay is detected by lithium-drifted germanium crystals, known as Ge(Li) detectors [Kno79]. They are typically biased with about 3500 V and passage of radiation through the semiconductor material creates ion pairs. The number of ion pairs produced and collected is proportional to the energy deposited by the gamma ray. The signal from the detector is converted into an event that is recorded in a multichannel analyzer. Our detectors are usually set to record gamma rays with energies of 60 keV to 2 MeV. After accumulating for a preset time, the spectra are stored by a minicomputer. The energy spectra are calibrated by use of a NBS standard gamma source, which can also be used to determine the efficiency of the detector, because the activities in the source were accurately known on the given reference date. The efficiency of the detector is a function of the distance from the detector and the energy of the radiation. It varies from a high of about 10% at 130 keV down to about 1% at 1 MeV and even lower at higher energies. The detectors are shielded by several inches of lead to reduce the level of background radiation from outside sources. However, the radiation from the sample itself causes background from Compton scattering and pair production, as well as from photon scattering on the sample holder and other nearby objects. The more activity there is in the vicinity of the

detector, the higher the background level. This is another reason to get the cleanest possible chemical fractions. Gamma ray spectra were accumulated for the Np, Pu, Am, Cm, and Bk fractions. The Cf and Es fractions from short bombardments were monitored for gamma radiation in order to determine cross sections for the production of ^{247}Cf and ^{250}Es.

To calculate the production cross section for a radionuclide, one needs the activity of that nuclide at the end of the bombardment (also known as the initial activity, or A_o), the target thickness, and the number of beam ions that passed through the target as a function of time. The samples are counted until the appropriate activities have decayed to negligible levels or until enough spectra have accumulated to give a good estimate of the initial activity attributable to an observed decay. In each spectrum, the peaks are integrated so one can determine an average activity at the midpoint of the counting interval. For alpha spectra, the level of background activity is low enough to allow one to merely sum the total number of counts in an isolated peak in order to determine its activity. If the peaks are close enough together, the low-energy tail of one peak will overlap the high-energy end of a lower-energy peak. Also, the thicker the source is, the wider the peak will be, and the more tailing there will be. The tailing can be approximated by assuming an exponential decrease on the low-energy side of an alpha peak. Gamma spectra are analyzed in a different manner because of the higher level of background radiation and a different peak shape than is seen in alpha spectra. For the gamma spectra, the background contribution to a peak is assumed to be linear and is fitted by average backgrounds on both sides of the peak. The calculated background is subtracted from the gross peak area to determine a net peak area. Calculated activities for a given peak in the spectra of a given sample are plotted as a function of time after end of bombardment. Depending on the nature of the decay (for example, one component, two component, or growth and decay) a least squares fit to the data is made by

use of the computer code FUTILE [Moo83]. The shape of the decay curve can be characterized by the A_o and the half-lives of the nuclides involved. FUTILE allows one to let the A_o's and half-lives of the decays vary or to be fixed at a user-chosen value. When the decay can be attributed to a given nuclide because of the characteristic energy and half-life, the half-life to be used by FUTILE can be fixed at the literature value. When the activity comes from the decay of a daughter nuclide, the time of chemical separation from the mother nuclide needs to be known.

The calculated A_o's must now be corrected for detector efficiency, chemical yield, and the branching ratio of the observed decay (the fraction of decays of that nuclide that decay by the observed alpha or gamma ray). Assuming a constant beam intensity over a time interval t, the production cross section for a radionuclide is given by:

$$\sigma = \frac{A_o}{(1-e^{-\lambda t}) \times I} \tag{4.1}$$

where σ is the cross section in cm^2, A_o is the corrected initial activity in disintegrations/sec, λ is the decay constant for the radionuclide produced, x is the target thickness in atoms/cm^2 and I is the flux of ions through the target in ions/sec [Mey67]. The beam intensity is rarely constant, however. We periodically recorded the beam integral during the bombardment. The beam intensity can be approximated by the average value over each of the recorded intervals. In this case, the production cross section is given by:

$$\sigma = \frac{A_o}{x \sum_{i=1}^{n} I_i \left(1 - e^{-\lambda(t_{i+1} - t_i)}\right) e^{-\lambda(t - t_{i+1})}} \tag{4.2}$$

where I_i is the average beam intensity over the time interval i, t_i is the time at the start of the interval i, and t is the time after the end of the bombardment.

The following table lists the radioactive properties of all nuclides observed in addition to a few that were searched for, but not found. The data include the nuclide, its half life, the energies of the observed radiations and the branching ratio of the most common gamma ray or the sum of the branching ratios of the most common alpha rays [TOI78].

Nuclide	Half life	Decay Energies	Branching Ratio
Np-238	2.117 ± .002 d	γ: 984, 1029 keV	27.8 %
Np-239	2.346 ± .004 d	γ: 106, 278, 228 keV	27.8 %
Pu-243	4.955 ± .003 h	γ: 84 keV	23 %
Pu-245	10.48 ± .05 h	γ: 327, 560 keV	26 %
Pu-246	10.85 ± .02 d (also observed Am-246m daughter)	γ: 224 kev	24 %
Am-239	11.9 ± .1 h	γ: 278 keV	15 %
Am-240	50.8 ± .3 h	γ: 988, 889 keV	73 %
Am-242g	16.01 ± .02 h (observed Cm-242 daughter)	β^-	82.7 %
Am-244g	10.1 ± .1 h	γ: 744, 898, 154 keV	66 %
Am-245	2.05 ± .01 h	γ: 253 keV	6.1 %
Am-246m	25.0 ± .2 m	γ: 1079, 799, 1062, 1036 keV	29.1 %
Am-246	39 ± 3 m	γ: 679, 205, 154, 756 keV	52 %
Am-247	24 ± 3 m	γ: 285, 226 keV	23 %
Cm-242	162.26 ± .04 d	α: 6.113, 6.070 MeV	100 %
Cm-249	65.3 ± .6 m	γ: 634, 560 keV	1.5 %
Bk-245	4.90 ± .03 d	γ: 253 keV	31.3 %
Bk-246	1.80 ± .02 d	γ: 799, 1082 keV	61.4 %
Bk-248g	23.5 ± .2 h	γ: 551 keV	4.6 %

Nuclide	Half life	Decay Energies	Branching Ratio
Bk-250	3.222 ± .005 h	γ: 989, 1029-32, 890 keV	45.2 %
Bk-251	55.6 ± 1.1 m	γ: 178 keV	5.2 %
Cf-245	43.6 ± .8 m	α: 7.137, 7.084 MeV	30 %
Cf-246	35.7 ± .5 h	α: 6.758, 6.719 MeV	99.8 %
Cf-247	3.15 ± .03 h	γ: Bk $K_{\alpha 1}$, $K_{\alpha 2}$	33.7 %
Cf-248	333.5 ± 2.8 d	α: 6.26, 6.22 MeV	100
Cf-250	13.08 ± .09 y	α: 6.031, 5.989 MeV	99.7 %
Cf-252	2.646 ± .004 y	α: 6.118, 6.076 MeV SF	96.7 % 3.092 %
Cf-253	17.82 ± .09 d (observed Es-253 daughter)	β^-	99.69 %
Cf-254	60.5 ± .2 d	SF	99+ %
Es-250g	8.6 ± .1 h	γ: 829, 303, 349 keV	73.6 %
Es-251	33 ± 1 h	α: 6.492, 6.462 MeV	0.49 %
Es-252	471.7 ± 1.9 d	α: 6.632, 6.562, 6.482 MeV	75.7 %
Es-253	20.47 ± .02 d	α: 6.633, 6.592, 6.552 MeV	100 %
Es-254m	39.3 ± .2 h (observed Fm-254 daughter)	β^-	99.59 %
Es-254	275.7 ± .5 d	α: 6.429, 6.416, 6.359 MeV	97.8 %
Es-255	38.3 ± .3 d (also observed Fm-255 daughter)	α: 6.30, 6.26 MeV	8 %
Fm-250	30 ± 3 m	α: 7.44 MeV	100 %
Fm-252	25.39 ± .05 h	α: 7.04 MeV	100 %
Fm-253	3.00 ± .13 d (also observed Es-253 daughter)	α: 6.943 MeV	6.41 %
Fm-254	3.240 ± .002 h	α: 7.187, 7.145 MeV	99 %
Fm-255	20.07 ± .07 h	α: 7.016, 6.96 MeV	100 %
Fm-256	2.627 ± .021 h	SF	91.9 %

5. Results

The calculated cross sections (in μb) for observed actinides are:

	^{132}Xe 817 - 793 MeV	^{129}Xe (hi) 791 - 769 MeV	^{129}Xe (lo) 723 - 700 MeV
Np-238	112 ± 15	32.7 ± 5.8	----------
Np-239	149 ± 17	48.5 ± 8.0	----------
Pu-243	608 ± 97	163 ± 34	27.6 ±16.0
Pu-245	321 ± 60	91.2 ± 17.9	135 ± 31
Pu-246	200 ± 19	41.7 ± 9.2	102 ± 67
Am-239	63 ± 19	----------	----------
Am-240	85.4 ± 7.5	83.8 ± 7.5	----------
Am-242g	271 ± 36	----------	----------
Am-244g	1410 ± 80	878 ± 52	160 ± 8
Am-245	3870 ± 370	1950 ± 200	240 ± 240
Am-246m	2110 ± 150	878 ± 148	----------
Am-246	2500 ± 360	1540 ± 310	----------
Am-247	6730 ± 1310	3170 ± 1160	----------
Cm-249	38110 ± 4150	29300 ± 3900	9300 ± 4000
Bk-245	345 ± 31	597 ± 85	108 ± 24
Bk-246	1150 ± 80	1570 ± 210	332 ± 44
Bk-248g	2540 ± 250	2810 ± 590	332 ± 90
Bk-250	3210 ± 180	2360 ± 140	599 ± 77
Bk-251	560 ± 119	----------	----------
Cf-245	4.32 ± 1.55	25.5 ± 7.4	----------
Cf-246	23.8 ± 3.1	79.1 ± 10.3	14 ± 7

	^{132}Xe 817 - 793 MeV	^{129}Xe (hi) 791 - 769 MeV	^{129}Xe (lo) 723 - 700 MeV
Cf-247	104 ± 22	----------	----------
Cf-248	499 ± 64	850 ± 122	450 ± 350
Cf-250	2690 ± 360	3600 ± 510	----------
Cf-252	273. ± 45.	477 ± 65	----------
Cf-253	13.3 ± 1.6	11.6 ± 1.5	11 ± 11
Es-250g	24.1 ± 6.0	----------	----------
Es-251	43.4 ± 15.8	----------	----------
Es-252	24.8 ± 3.0	40.8 ± 5.1	7.78 ± 1.83
Es-253	10.66 ± 1.16	13.2 ± 1.6	2.20 ± .30
Es-254	5.93 ± .78	4.83 ± .70	----------
Es-254m	1.79 ± .20	1.57 ± .21	.252 ± .047
Es-255	.526 ± .070	.429 ± .082	----------
Fm-252	1.02 ± .31	< 5.92 ± .73	1.12 ± .52
Fm-253	1.45 ± .28	4.70 ± .75	.84 ± .16
Fm-254	.83 ± .11	.48 ± .08	.32 ± .08
Fm-255	.36 ± .15	----------	----------
Fm-256	.093 ± .018	.188 ± .056	----------

For the ^{129}Xe(lo) bombardments, the beam intensity was lower than during the other experiments. As expected, the production cross sections are smaller than those from the ^{129}Xe(hi) bombardments, because the incident energy is lower. Problems which arose during the separations of the Cf fraction and the short-lived Am fraction limited the accuracy of the determination of those cross sections.

In the long ^{132}Xe and ^{129}Xe(hi) bombardments, we placed a catcher foil on the beam stop to collect products recoiling from the target along the beam

direction. A berkelium fraction was separated and Bk-245,246 were detected by their gamma decays. The following cross sections are upper limits for the production of these nuclides. The small cross-sections indicate that the conical catcher foil system used caught most of these products.

	Zero Degree Foils	
	^{132}Xe	$^{129}Xe(hi)$
Bk-245	.012 ± .012 mb	.022 ± .006 mb
Bk-246	.022 ± .010 mb	.040 ± .007 mb

6. Discussion of Results

The cross sections for actinide products from the three systems studied in this work are plotted as a function of mass number A in Figures 6.1, 6.2, and 6.3. Figure 6.4 shows the actinide cross sections from $^{136}Xe + ^{248}Cm$ [Moo83] at 790 - 699 MeV on target. This large energy range is due to the thicker target used, 2.15 mg/cm^2 ^{248}Cm as CmF_3. Also, since lighter media have larger stopping power [Hub80], the proportionally more light material in CmF_3 compared with Cm_2O_3 makes the energy loss in the target for $^{136}Xe + ^{248}Cm$ larger. The ^{136}Xe energy range is large enough to cover the energies on target for both the ^{129}Xe(hi) and ^{129}Xe(lo) experiments. When comparing the elemental production cross sections from the three different projectiles, we see that the widths and the peak positions of the distributions change, as well as the total cross section for production of a given element. Due to the determination of fewer cross sections, the only conclusion to draw from the ^{129}Xe(lo) bombardments is that the production cross sections are smaller than from ^{129}Xe(hi), as expected. The Pu-245, 246 cross sections, however, are larger at the lower bombarding energy. Excitation functions of Pu isotopes from $^{136}Xe + ^{248}Cm$ [Moo83] show the expected increase in production cross section with increasing energy on target. It would have been helpful to have determined cross sections for the neutron-rich Am isotopes from the ^{129}Xe(lo) reaction to see if the production cross sections for neutron-rich below target nuclides decrease less rapidly with decreasing energy on target when using a neutron deficient projectile.

For reactions occurring at energies nearly equal to the Couloumb barrier, the production cross sections should increase with increasing bombarding energy. Because of energy loss in the target, there is a spread in projectile energies on target, and the higher energies contribute more to the overall production than do the lower energies. If the energy dependences of the cross sections are

not the same for different elements, the relative difference in cross section between two elements depends on the energy range of the projectiles in the target. The relatively poor data from the ^{129}Xe(lo) reaction prevents one from reaching any conclusions concerning relative cross sections for products formed in the ^{129}Xe(hi) and ^{129}Xe(lo) reactions.

Figures 6.5 - 6.10 show production cross sections for Np-Pu, Am, Cm-Bk, Cf, Es, and Fm, respectively, as a function of projectile used in the high energy bombardments. The peak in the cross section for a given element shifts to a lower mass number as the projectile is changed from ^{136}Xe to ^{132}Xe to ^{129}Xe. This effect is most apparent in the Fm, Bk and Pu data. For the above-target products, the overall trend is the shift to lighter masses along with an increase in total element production. We cannot determine a peak shift for Cf because of the absence of data for the cross sections for the long-lived Cf-249,251, both of which should have cross sections among the highest for Cf isotopes. The calculated production cross section for ^{250}Cf has not been corrected to account for feeding during the bombardment due to β^- decay of the short lived ^{250}Bk. As a result, the listed production cross section of ^{250}Cf is larger than its actual value. The neutron-deficient Es isotopes (Es-249,250,250m and 251) all decay principally by electron capture and are detected by gamma ray emission. As explained in Section IV, the minimum gamma ray activity needed to see a decay is higher than for an alpha particle decay, and an insufficient number of the neutron-deficient einsteinium nuclides are made to allow us to observe any peak position changes. The listed production cross section for ^{254}Es may be inaccurate due to contamination from its occasional use as a source for calibration of elution positions of actinides on ion exchange columns. When the einsteinium data are plotted, only the ^{254m}Es cross section is shown. An interesting and surprising feature of the above-target production is that the cross sections for the production of the most neutron-rich nuclides formed, such as Cf-253,254, Es-254,255,

and Fm-255,256, are independent of the projectile.

The only curium isotope production cross section determined in any experiment was for ^{249}Cm. The other curium isotopes are too long-lived, have no strong gamma decays, or are undetectable in an alpha spectrum of a curium sample due to a large amount of activity from target material that has been transferred to the catcher foil due to coulomb interactions and energy loss (appearing as heat) in the target from the projectiles. Cm-249 represents the addition of one neutron into a target nucleus. It is not surprising that the experimentally determined cross section for Cm-249 increases as the number of neutrons in the projectile increases. Characteristics of below-target production are sketchier because of fewer nuclides detected. All three below-target elements observed (Np,Pu,Am) show decreased production as the projectile gets lighter. Only Pu nuclides show the expected peak shift. There are not enough Np data to determine if a peak shift has occurred. The production cross sections for Am isotopes produced by large transfers are largest using ^{129}Xe, but for the 1-3 nucleon transfers, ^{136}Xe forms the most products. The distribution of cross sections arises from a sum of distributions from the two mechanisms, QE and DIR. For Am, a narrow gaussian distribution peaked near Am-247 comes from QE while a lower, wider gaussian peaked at a smaller mass number comes from DIR. The cross sections for the production of ^{247}Am from ^{136}Xe due to QE reactions are the largest of those from the three projectiles because ^{136}Xe has the largest mass number and because it would be easier to transfer a proton to the neutron-rich (proton-poor) ^{136}Xe than to the neutron-poor (proton-rich) ^{129}Xe. The cross sections due to DIR are smaller and the maxima shift to lower mass numbers with the more neutron-poor projectiles.

In order to describe the features of the cross sections for the production of target-like products, especially those nuclides produced by DIR, a potential

energy surface (PES) has been found to be a helpful tool. The distribution of primary products (that is, the products present before deexcitation through neutron evaporation or fission) depends on the relationship between nucleon rearrangement and the forces acting on the nucleons. The most probable mass distribution should occur when the density of states in the dinuclear complex is largest, which corresponds to a minimum of the potential energy of the system [Gro81]. For a given pair of primary products the potential energy used is the sum of their ground state masses plus the coulomb, nuclear and centrifugal potentials, evaluated at some separation distance, usually one corresponding to touching spheres.

$$V = V(\text{mass}) + V(\text{coul}) + V(\text{nuc}) + V(\text{cent}) \tag{6.1}$$

The PES is a plot of the difference in potential energy (PE) between product pairs and the two reactants and shows the effect of net nucleon flow on available energy.

$$PE = V(\text{prod}) - V(\text{react}) \tag{6.2}$$

The largest contribution to the potential energy comes from the ground state mass differences, denoted by Q_{gg}.

$$Q_{gg} = \text{mass}(\text{react}) - \text{mass}(\text{prod}) \tag{6.3}$$

A positive PE, as defined in eqn 2, for a given pair of products means that energy is needed to produce the required nucleon flow to make those products. If the PE is too large, the products cannot be made.

Excitation energy, E^*, of the products is indirectly related to PE through the kinetic energy lost during the interaction:

$$E^* = (KE_{in} - KE_{out}) + Q_{gg} \tag{6.4}$$

where KE_{in} and KE_{out} are the initial and final kinetic energies of the products in

the center-of-mass frame. Kinetic energy loss is a function of the interaction time, which implies a dependence on the impact parameter for a given interaction.

Many researchers have shown that the PES accurately describes the evolution of primary products in heavy ion reactions [Fre84]. The systems studied cover a wide range in mass and include $^{132}Xe + ^{56}Fe$ [Heu78], $^{144}Sm + ^{144}Sm$ and $^{154}Sm + ^{154}Sm$ [Wu81] and $^{238}U + ^{238}U$ [Fre79]. The centroid of the primary product distributions follows the gradient of the PES, beginning from the target- projectile combination (the injection point). The interaction time determines how far the system travels along the PES. As pointed out earlier, N/Z equilibration occurs quickly, and is represented on the PES by a drift down the steep walls into the valley of the PES, which runs near, but not necessarily along, the valley of beta stability. Once in the valley, the system then drifts toward equilibration of the mass asymmetry mode (toward compound nucleus formation or toward formation of two equal mass products). In support of this, the experimentally determined path of the first moments of the projectile-like nuclide distribution in the reaction of 800 MeV $^{136}Xe + ^{56}Fe$ was shown to closely follow the gradient of the PES when the observed nuclides were corrected for neutron evaporation [Sch81]. The general shape of equipotential curves is of long narrow ellipses aligned along the valley of the PES. The ellipses are often kinked at neutron or proton numbers which correspond to closed shells in the projectile or the target.

Shell effects on the PES were shown to be important in the $^{144}Sm + ^{144}Sm$ and $^{154}Sm + ^{154}Sm$ reactions. For $^{144}Sm + ^{144}Sm$, the injection point is a local minimum on the PES mainly because both the target and projectile contain a closed shell of 82 neutrons. On the PES in the vicinity of Z=62 (Sm), the minimum of the PES for a given Z is displaced away from the N/Z ratio of the

^{144}Sm and toward N=82, due to the shell. The initial drift of mass in the reaction follows the shape of the PES and causes products to be more neutron-deficient (rich) for Z > (<) 82 than can be expected from using the N/Z of ^{144}Sm. The data from the ^{154}Sm + ^{154}Sm reaction can be analyzed in a similar fashion.

The computer program HEAVI was written to calculate the potential energy surface for production of target-like nuclides for a heavy ion reaction at a given projectile laboratory energy and angular momentum. The mathematical forms of the nuclear, coulomb, and centrifugal potentials used in the calculation are from "Heavy Ion Fusion: Comparison of Experimental Data with Classical Trajectory Models" by Birkelund et.al.[Bir79]. That work involved solving mechanical equations of motion to determine if the nuclei get close enough to permit fusion. These equations of motion also include terms which evaluate energy loss due to friction, using a one-body proximity form [Ran78]. I chose not to include friction terms in HEAVI. The nuclear potential used is a proximity potential [Blo77], and the coulomb potential is a phenomenological one developed by Bondorf [Bon74]. The masses used in the calculation of the PES were either the actual ground state masses or were calculated shell-corrected, liquid droplet masses of Myers [Mye77]. In the actinide region, the calculated liquid droplet mass is often 1.0-1.5 MeV less than the actual ground state mass. For a mass chain A, a least-squares parabolic fit was made of the difference between the actual mass (from the Table of the Isotopes [TOI78]) and the calculated liquid droplet mass as a function of Z. These small corrections are added into the calculated liquid droplet masses to get more accurate values for ground state masses of unknown nuclides as well as to give better approximations for known nuclides. Use of the actual ground state masses causes kinks in the PES due to the even-odd effect. Calculated liquid droplet masses without the even-odd term give a smoother surface, and as long as the excitation energy of the primary products is not too large (< 40 MeV), shell corrections still affect the mass of the participants. Neither

calculated liquid droplet nor actual masses reflect the deformation of the participants that occurs during the interaction and subsequent break-up.

In the calculation of the PES, the various potentials are evaluated at the interaction radius for the reactants. This separation distance is a function of the masses of the 2 participants. The sum of these potentials and the ground state masses of the reactants constitutes the entrance channel potential. Next, for each possible product pair, a new separation distance is calculated (reflecting the mass transfer needed to make the particular products) and the exit channel potential is calculated from the various potentials, reevaluated at this new separation distance.

Shell effects in nuclei affect the calculation of the PES only through Q_{gg}. As pointed out earlier, the value of the PES is additionally decreased along neutron or proton numbers equal to magic numbers. If the projectile or target has a magic number of neutrons or protons, the injection point of the system is usually at a local minimum on the PES. Otherwise, the system evolves along the gradient of the PES to a local minimum. Once there, the movement of nucleons involves statistical fluctuations. The steepness of the walls of the PES around the local minimum influences the spread of the element distribution of products formed after arrival of the system at the minimum [Gro80]. The spread is measured as the second moment (σ_z^2) of a gaussian used to fit element product distributions as a function of the total kinetic energy loss (TKEL) involved. For example, the injection point for the $^{208}Pb + ^{208}Pb$ reaction, where both participants are doubly magic, is at the overall minimum of a deep well on the PES. In this system, a very large TKEL is associated with an increase of σ_z^2 from 0 to 10 [Tan80], implying that the shells inhibit nucleon exchange. The PES for systems that involve fewer magic numbers or start further from magic numbers are shallower, and the TKEL becomes associated with larger σ_z^2, meaning nucleon

exchange is easier. A study of the $^{238}U + ^{238}U$ showed such features [Hil77].

Figures 6.11, 6.12 and 6.13 show the calculated potential energies for target-like products for, respectively, 780 MeV ^{129}Xe, 805 MeV ^{132}Xe, and 745 MeV ^{136}Xe with ^{248}Cm. Figures 6.14, 6.15, and 6.16 are contour plots of the same potential energy surfaces. The contours are 2 MeV apart and the injection point is denoted by a "+" . One feature common to all 3 PES is the sharp rise in potential for Z>100 due to the Z=50 shell, as well as a kink corresponding to N=82 in the projectile-like fragment. As the projectile neutron number decreases from the N=82 shell in ^{136}Xe, the injection point moves higher up the slope of the PES and the minimum of the PES for a given Z near 96 in the target-like product is at N corresponding to N=82 in the projectile-like product. The path along the gradient of the PES from the injection point for the three xenon isotopes explains one aspect of the observed production cross sections. For ^{129}Xe and ^{132}Xe, the initial drift of the target-like masses is toward higher Z and smaller N products. As a consequence, the above target production increases at the expense of the below target production. After reaching the bottom of the valley of the PES, the system should then drift toward mass symmetry. For ^{136}Xe, the injection point is within 1 MeV of the lowest point on the surface and therefore, the product mass distributions spread out from the target's proton and neutron numbers.

The bombarding energy and impact parameter for a given nuclear interaction determine the interaction time and consequently, how far the system moves along the path on the PES. Because of the rotational energy contribution to the PES, each different impact parameter yields a slightly different PES. When calculating the PES for the reactions studied, an initial angular momentum of 150 $\hbar$ was chosen. This corresponds to about 0.7 times the grazing angular momentum for the higher energy bombardments.

The separation distance R used in HEAVI is the interaction radius R_{int}, which

corresponds to the separation distance of the reactants where elastic scattering changes to nuclear reactions [Wil80]. R_{int} is mathematically related to the matter half density radii C_p and C_t for the reactants as follows:

$$R_{int} = C_t + C_p + 4.49 - (C_t + C_p)/6.35 \quad fm \tag{6.5}$$

$$C_i = R_i * (1 - (1/R_i)^2) \quad fm \tag{6.6}$$

$$R_i = 1.28 * A_i^{1/3} - 0.76 + 0.8 * A_i^{-1/3} \quad fm \tag{6.7}$$

where R_i is the equivalent sharp radius for a nucleus of mass number A_i. Other possible choices for a separation distance include the sum of the equivalent sharp radii $R_t + R_p$, and

$$R = 1.36 * (A_1^{1/3} + A_2^{1/3}) + .5 \quad fm \tag{6.8}$$

which comes from a fit to R-values derived from reaction cross sections [Wil73]. However, as shown in Table 1, the choice of R does not affect the calculated potential energy surface significantly because the PES is the difference between the potentials for the products and reactants at the given R. The magnitude of the PES changes slightly, but the calculated position of the minimum of the PES does not change. The calculated excitation energy of the products formed by a DIR mechanism is sensitive to the choice of R, because the products are assumed to separate with an energy attributable to the coulomb repulsion of 2 spheres whose centers are separated by a distance R. Therefore, the calculated excitation energy increases for larger values of R.

It has been noted [Mer83] that mass distributions in high energy heavy ion reactions often cannot adequately be analyzed by use of a static PES, the kind used here. Deformation due to high excitation energies is one effect whose contribution to the PES has not been included. However, all the bombardments done here were at energies slightly above the barrier, and the PES has been shown to

be useful in this energy regime.

Other researchers have claimed that the peak in the primary cross section distributions <A> for a given element produced primarily by DIR is indicated by the minimum of the PES for that Z [Sch82]. The difference between <A> and the observed peak in cross sections <A'> indicates the average number of neutrons emitted during deexcitation, and provides as well an estimate of the excitation energy of these surviving products. All of those reactions, though, involved neutron-rich projectiles and targets. Table 2 summarizes the Bk to Fm cross section maxima as predicted by the PES and by the N/Z ratio of the combined system. Also shown are the actual peak positions and the mass weighted excitation energy of the nuclide at the peak. The calculated PES for the reaction of ^{129,132}Xe on ^{248}Cm predicts the peak in the primary distributions for Fm and Es products to be at a smaller A than is actually observed for the final products. Lack of a cross section for the production of ^{250}Fm from the reaction with ^{129}Xe prevents the determination of the peak for Fm, but the data indicate a peak near ^{252}Fm, since the distribution appears to be leveling off at that position. The Bk and Cf distributions also peak at a higher mass than predicted, but since QE is a significant mechanism for these small transfers, it is not surprising that the peaks are at mass numbers near that of the target, making them much larger than those resulting from PES predictions.

There are not many mechanisms that result in a primary distribution moving to higher mass numbers following deexcitation. One possibility is that the more neutron-deficient isotopes have much more excitation energy than do the heavier ones, thereby severely depleting the neutron-poor side through the loss by fission. The total excitation energy for the 2 products, assuming a DIR mechanism, was given by Eqn. 4. The kinetic energy after the reaction is assumed to result from the coulomb repulsion of the 2 touching products. For

Fm products from ^{129}Xe(hi), the total excitation energy for the 2 products is nearly constant, at about 29-34 MeV, for ^{248}Fm to ^{256}Fm. If the excitation energy is split among the products proportional to their mass, the Fm gets about 22 MeV. The range in excitation energy does not appear to be large enough to cause preferential depletion of the lighter isotopes, unless the energy split among the products favors highly excited neutron-poor Fm along with cold neutron-rich ones. Another possibility is that the reactants did not stay in contact long enough. The mass distribution modes for the combined system may not have reached equilibrium values (the minima of the PES) and this would leave a distribution that was more neutron-rich than expected.

Finally, QE may contribute more than originally expected to these $\Delta Z=4$ transfers. For ^{129}Xe + ^{248}Cm, QE would produce a more neutron-rich distribution of Fm than would DIR. Since we did not find any Fm isotopes lighter than ^{252}Fm, the DIR contribution could be centered at ^{250}Fm, as predicted by PES, but the QE contributions in the heavier Fm's could make the final distribution the one that we see.

This possibility is supported by conclusions drawn from bombardments of ^{197}Au by 761 MeV ^{129}Xe, 764 MeV ^{132}Xe and 787 MeV ^{136}Xe at energies near the barrier [Kra79]. In that work, radiochemical techniques were used to determine production cross sections for target- and projectile-like products, as well as those nuclides formed by the fissioning of excited target-like fragments. The mass yields of elements near the target or projectile were deconvoluted into QE and DIR distributions. The low spin isomers of near reactant nuclides were assumed to be formed principally by QE reactions, while the high spin isomers and the more neutron deficient products were the result of a DIR mechanism. Production due to QE drops rapidly as the net number of protons transferred increases. Because product cross sections were determined for both target- and

projectile-like nuclides, the number of neutrons emitted by the complementary fragments during deexcitation could be calculated.

The QE products appeared to be formed with little excitation energy, because the sum of the mass numbers at the peaks of the QE cross section distributions for complementary products equalled the sum of the mass numbers of the reactants. For the DIR products, the missing mass increases with the net increase of transferred nucleons, implying higher excitation energies, more kinetic energy loss, and longer interaction times. The mass number of the peak of the DIR distribution after deexcitation by neutron evaporation for a given Z could be accurately predicted by assuming the excitation energy was split among the 2 products in proportion to their masses and by using a potential energy surface. Inclusion of shell corrections for the masses used in the PES resulted in better fits for damped products with excitation energies of > 50 MeV. It should be noted that the N/Z ratio of the maxima of the DIR elemental distributions is poorly predicted by assuming the N/Z ratio of the products is equal to the overall N/Z ratio of the combined system.

As expected, the use of the more neutron deficient projectile in the Xe + Au reactions produces a more neutron deficient distribution of products. A comparison of the PES's for the three Xe + Au systems shows that the injection point for all three systems is only a few MeV above the bottom of the PES. Also, the ratio of above target element production to below target element production should be nearly constant for all three projectiles, since the gradient of the PES from the injection point is rather small. These conclusions have been experimentally verified by analysis of the bombardment of ^{197}Au with 900 MeV ^{132}Xe [Kra81]. The integral element yields of damped products from 6.37 MeV/A ^{132}Xe + ^{197}Au and from 7.2 MeV/A ^{136}Xe + ^{197}Au [Rus77] show the same element distribution (after the ^{136}Xe data were normalized to the ^{132}Xe data at Z = 79).

Also, above target production is only slightly larger than below target production. For bombardments with the different xenon isotopes at the same energy, the projectile with the largest mass number should have the largest total reaction cross section and therefore the largest QE cross section (since the DIR contributions from the three different isotopes are the same).

The total reaction cross section σ_r for heavy ion reactions can be estimated by:

$$\sigma_r = 10\,\pi\,R_{int}^2\left(1-\frac{V_c\,(R_{int})}{E_{cm}}\right)\quad mb \qquad (6.9)$$

where R_{int} is the interaction radius in fm, $V_c(R_{int})$ is the coulomb potential in MeV evaluated at R_{int}, and E_{cm} is the incident energy in MeV in the center-of-mass reference frame [Nor80]. The factor of 10 scales σ_r to millibarns. If the target is thick enough to degrade the energy of the projectiles as they pass through it, a modified expression for the calculation of σ_r is used:

$$\sigma_r = 10\,\pi\,R_{int}^2\left(\frac{1}{E_1-E_2}\right)\int_{E_2}^{E_1}\left(1-\frac{V_c(R_{int})}{E}\right)\,dE\quad mb \qquad (6.10)$$

where E_1 is the incident energy and E_2 is the energy of the projectile (both in the center of mass frame) after passing through the target [Kra76]. The beam energy is often reduced to a value below that of the coulomb barrier, in which case no nuclear reactions take place. E_2 is then equal to $V_c(R_{int})$.

After calculating σ_r, the quasi-elastic cross section (σ_{QE}) can be approximated by assuming that the critical phenomenon determining the mechanism to be followed during a nuclear interaction is the contact time of the reactant nuclei [Wes83]. The critical merging time of the reactants is derived to be:

$$t_m = 2.6 \times 10^{-23} A^{1/2} \left(\frac{A_T A_P}{A^2}\right)^{1/3} \left(\left(\frac{A_T}{A}\right)^{1/3} + \left(\frac{A_P}{A}\right)^{1/3}\right) \text{ sec} \quad (6.11)$$

where t_m is the merging time, A_t and A_p are the mass numbers of the target and projectile and $A = A_t + A_p$. The impact angular momentum l which causes the separation distance of the reactants to be less than R_{int} for the time t_m is used to calculate σ_{QE}:

$$\sigma_{QE} = \sigma_r - 10\pi \frac{(\hbar\, l(t_m))^2}{2\mu E_{cm}} \quad \text{mb} \quad (6.12)$$

The value of R_{int} used in [Wes83] was calculated as:

$$R_{int} = C_T + C_P + 2.97 \quad \text{fm} \quad (6.13)$$

where C_T and C_P are calculated from Eqn. 6.6. For $l < l(t_m)$, the nuclei overlap sufficiently to characterize the reaction as DIR. Table 3 shows the calculated σ_r, σ_{QE}, and σ_{DIR} for Xe-129,132, and 136 + Cm-248 and Au-197 reactions, along with experimentally determined σ_{QE} and σ_{DIR} for the $^{129}Xe + ^{197}Au$ reaction. For these low energy reactions, QE accounts for about half of the reaction cross section of the primary distribution.

As shown in the Xe + Au bombardments, the QE mechanism produces nuclides with little excitation energy, while the DIR products have much more, although there is a range of possible excitation energies. For actinide products, fission is a very favorable deexcitation mode for primary products. The products with large E^* (from DIR) will be strongly depleted by fission, while the QE products will be proportionally less depleted. For the ^{129}Xe and ^{132}Xe projectiles, the primary DIR product distribution for a given Z peaks at a smaller A than does the QE. However, the depletion by fission of the DIR makes the final distributions peak at higher mass numbers than would be predicted by the PES because of the

less depleted QE contribution. For the neutron rich projectiles, like ^{136}Xe and ^{48}Ca, the DIR product distribution peaks at mass numbers close to where the QE products peak, and so fission depletion of the DIR products does not affect the peak position of the final products as much. In the primary product distribution, the QE contribution is greater than the DIR contribution for $\Delta Z \leq 2$. The Pu, Am, Bk, and Cf products show that most of these final products are formed by the QE mechanism, as evidenced by where those distributions peak. The DIR contribution is indicated by the presence of nuclides such as ^{240}Am and $^{245,246}Cf$. These products can be formed cold (i.e. with little E^*) or by the evaporation of neutrons (without any fission) from a heavier isotope with considerable excitation energy. The determination of production cross sections for projectile-like products could help decipher the energy distribution. However, because the target system used requires the projectiles to pass through many materials before reaching the target, there are many ways to make projectile-like products. Also, the neutron-rich projectile-like products have the same mass numbers as fission products of the target-like products. Therefore, no chemical separation of projectile-like products was performed.

Finally, the projectile-independent cross sections for the neutron rich Cf, Es, and Fm nuclides is a consequence of the shift of the centroid of the distributions to lighter A and larger cross sections as the neutron number of the projectile decreases. These two effects offset each other in this region. If the even more neutron rich nuclides such as Cf-254,255, Es-256 and Fm-257 had been observed, ^{136}Xe would probably have made more of them than would ^{132}Xe or ^{129}Xe.

7. Conclusions

The potential energy surface has been shown to be effective in predicting the trends in actinide product cross section distributions for the three xenon isotopes (^{129}Xe, ^{132}Xe, ^{136}Xe) used as projectiles in these heavy ion reactions with ^{248}Cm. The actinide product distributions are a sum of distributions from the two reaction mechanisms, quasi-elastic (QE) and deep inelastic reactions (DIR). The QE distribution is strongly peaked at A and Z values near those of the target and projectile. These products are formed with relatively little excitation energy. The minimum of the potential energy surface (PES) for a given Z should be the maximum of the primary distributions of the DIR products. The small fission barriers for actinide nuclei allow fission to be the primary deexcitation mode for the products with excitation energy. Therefore, the DIR products are more heavily depleted by fission than are QE products. For the more neutron deficient projectiles, the DIR distributions peak at much smaller A than do the QE distributions. So, the maxima in the product cross section distributions for $\Delta Z \geq 3$ can appear at mass numbers greater than that predicted by the PES, because the DIR contribution has been reduced to a size comparable to the QE contribution. For the neutron rich projectile, ^{136}Xe, the two mechanisms give distributions that peak at similar A values, so the depletion of the DIR products does not cause a large shift to higher mass numbers. In fact, the distribution may shift to lighter mass numbers due to the fact that those DIR actinide products which did not fission must have evaporated neutrons to deexcite.

The PES also predicts that above target nuclide production increases with the more neutron deficient projectiles at the expense of the below target production. However, most of the increase goes into the neutron deficient products, limiting the usefulness of the ^{129}Xe and ^{132}Xe projectiles in making new neutron rich products.

Figure Captions

3.1) Exploded view of the target system used at the SuperHILAC.

4.1) A brief description of the rapid chemical separation procedure used to isolate short lived Bk, Cf, Es, Fm, and Md nuclides produced during short bombardments of ^{248}Cm is shown. These samples are suitable for α- or γ-ray pulse height analysis.

4.2) A brief description of the rapid chemical separation procedure used to isolate short-lived Am nuclides produced during short bombardments of ^{248}Cm is shown. The sample generated is suitable for only γ-ray analysis.

4.3) An outline of the chemical separation procedure used for the separation of fractions of U through Md from long bombardments of ^{248}Cm is given.

6.1) Production cross sections in millibarns of actinide nuclides formed in the reaction of 791 - 769 MeV ^{129}Xe with ^{248}Cm.

6.2) Production cross sections in millibarns of actinide nuclides formed in the reaction of 723 - 700 MeV ^{129}Xe with ^{248}Cm.

6.3) Production cross sections in millibarns of actinide nuclides formed in the reaction of 817 - 793 MeV ^{132}Xe with ^{248}Cm.

6.4) Production cross sections in millibarns of actinide nuclides formed in the reaction of 790 - 699 MeV ^{136}Xe with ^{248}Cm.

6.5) Np and Pu production cross sections from ^{129}Xe(hi), ^{132}Xe, and ^{136}Xe with ^{248}Cm.

6.6) Am production cross sections from ^{129}Xe(hi), ^{132}Xe, and ^{136}Xe with ^{248}Cm.

6.7) Cm and Bk production cross sections from ^{129}Xe(hi), ^{132}Xe, and ^{136}Xe with ^{248}Cm.

6.8) Cf production cross sections from ^{129}Xe(hi), ^{132}Xe, and ^{136}Xe with

^{248}Cm.

6.9) Es production cross sections from ^{129}Xe(hi), ^{132}Xe, and ^{136}Xe with ^{248}Cm.

6.10) Fm production cross sections from ^{129}Xe(hi), ^{132}Xe, and ^{136}Xe with ^{248}Cm.

6.11) Calculated Potential Energy Surface (PES) for 780 MeV ^{129}Xe + ^{248}Cm, with l = 150 ħ. The masses used are calculated liquid droplet masses corrected with a least squares fit to actual masses, but without the even-odd term included.

6.12) The calculated PES for 805 MeV ^{132}Xe + ^{248}Cm, with l = 150 ħ. Same modifications in mass are used as in Fig. 11.

6.13) The calculated PES for 745 MeV ^{136}Xe + ^{248}Cm, with l = 150 ħ. Same modifications in mass are used as in Fig. 11.

6.14) Contour plot of PES for 780 MeV ^{129}Xe + ^{248}Cm (fig. 11). Contours are 2 MeV apart. Injection point (target Z and N) is indicated with a " + ". The curve starting at the injection point is along the gradient to the PES. The centroid of the primary distribution of target-like products moves along this path as a function of increasing interaction time.

6.15) Contour plot of PES for 805 MeV ^{132}Xe + ^{248}Cm. See figure 14.

6.16) Contour plot of PES for 745 MeV ^{136}Xe + ^{248}Cm. See figure 14. Note that the injection point is within MeV of the lowest point on surface.

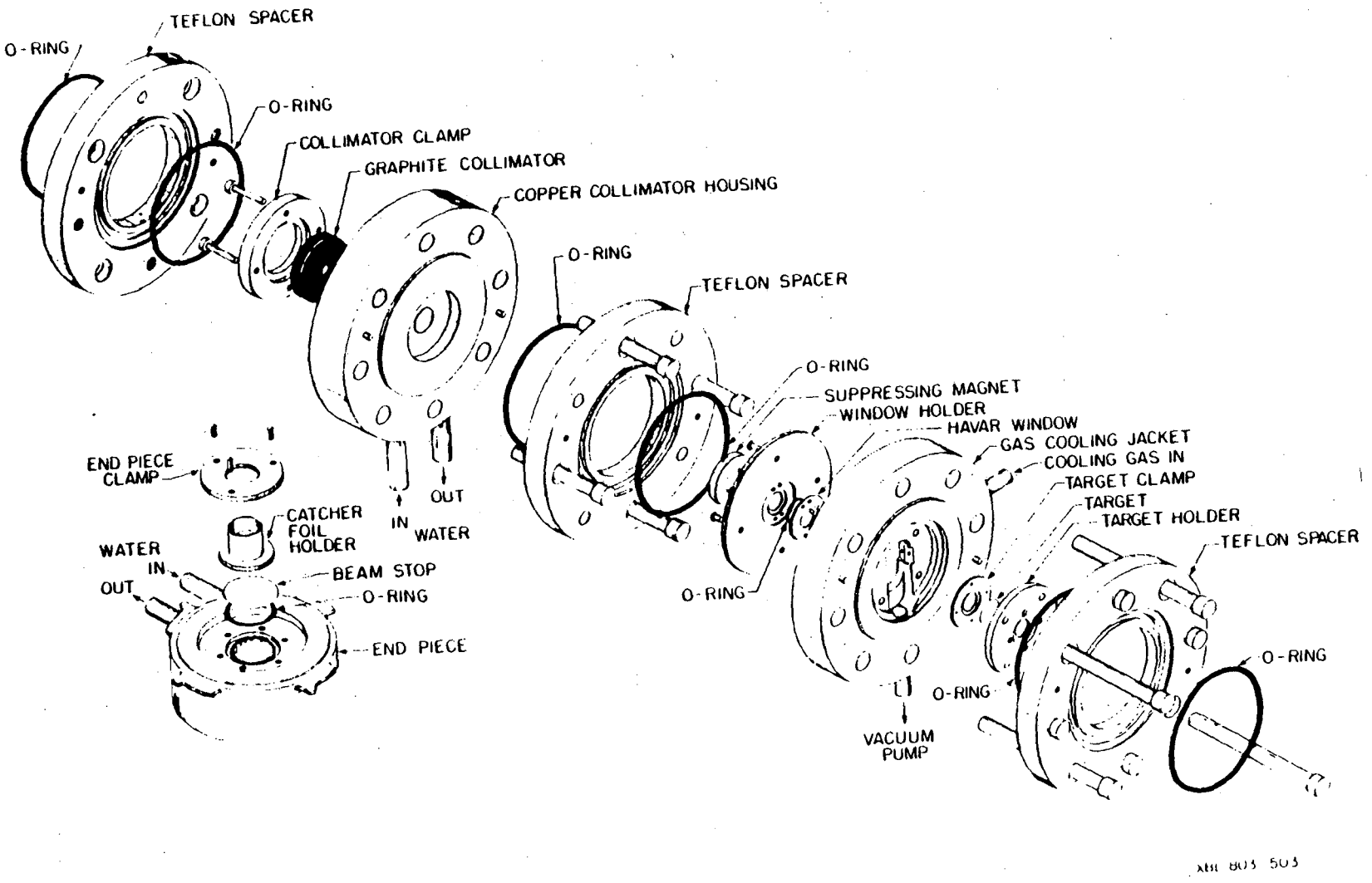

XBL 803 503

Figure 3.1

Rapid Bk-Md Separation

Gold Catcher Foil with Reaction Products

- dissolve with aqua regia
- extract Au with diethyl ether
- load on cation column
- elute, in order: Md, Fm, Es, Cf, Bk with pH 3.7 α-HIBA
- plate on Pt disc, flame, α count

Figure 4.1

Rapid Chemical Separation Procedure for Americium

Al Catcher Foil with Reaction Products

- Dissolve with 10M NaOH (including ^{241}Am tracer)
- dilute, add La^{+3} carrier,
- $La(OH)_3$ precipitates
- wash precipitate with 1M NH_4OH
- Dissolve precipitate with 1M HNO_3
- add .2M $S_2O_8^{-2}$, 1 drop 10 % $Ag(NO_3)$ solution
- heat

$Am(III) \longrightarrow Am(VI)$

- add 1M NH_4F

LaF_3 precipitate — discard

Am(VI) in solution

- add $Mn(NO_3)_2$

$Am(VI) \longrightarrow Am(III)$

- add La^{+3}

$\underline{LaF_3}$ (with Am)

- collect on filter frit

Figure 4.2

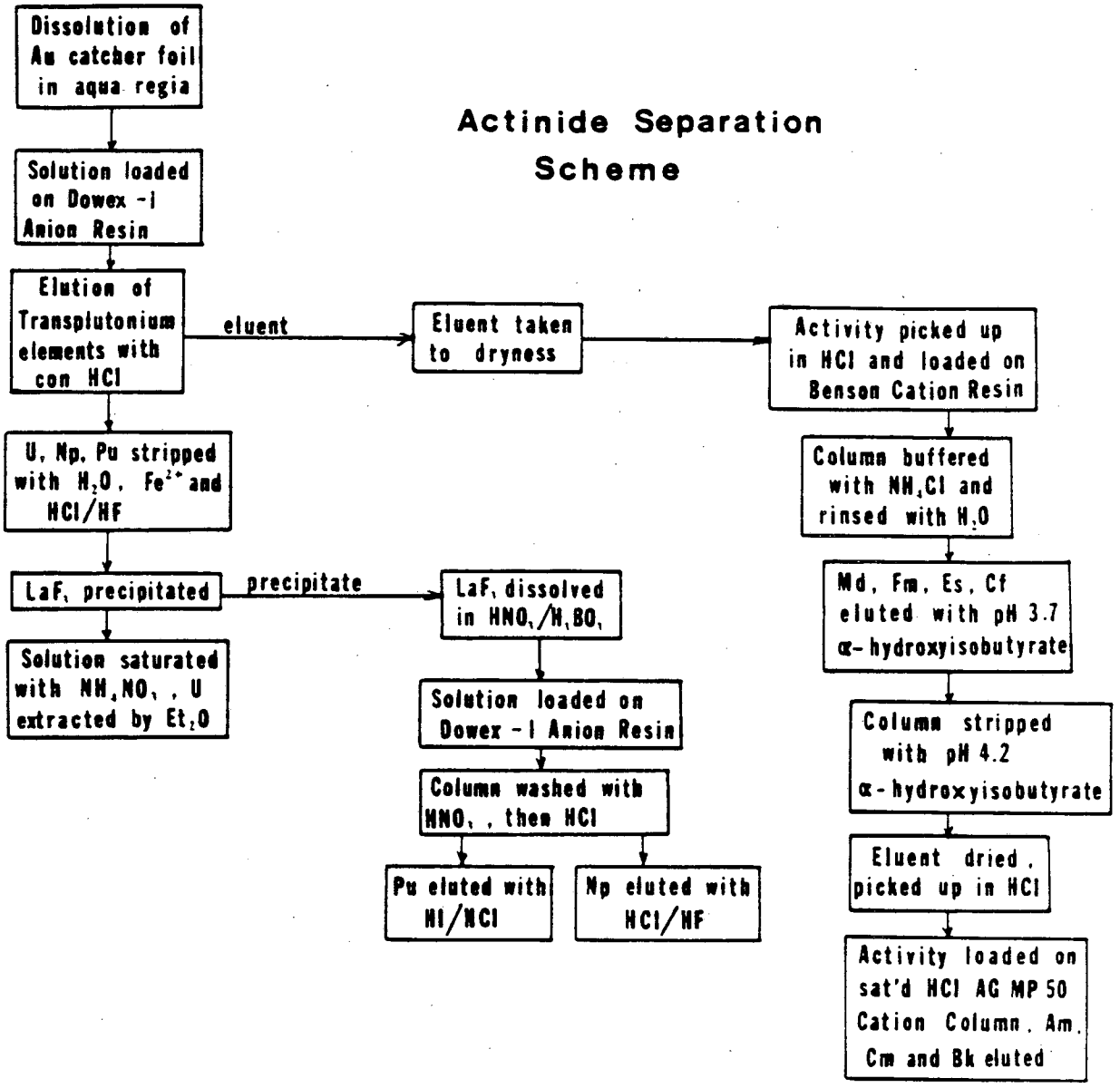
Actinide Separation Scheme
Dissolution of Au catcher foil in aqua regia
Solution loaded on Dowex -1 Anion Resin
Elution of Transplutonium elements with con HCl
eluent
Eluent taken to dryness
Activity picked up in HCl and loaded on Benson Cation Resin
U, Np, Pu stripped with H_2O, Fe^{2+} and HCl/HF
Column buffered with NH_4Cl and rinsed with H_2O
LaF_3 precipitated
precipitate
LaF_3 dissolved in HNO_3/H_3BO_3
Solution saturated with NH_4NO_3, U extracted by Et_2O
Md, Fm, Es, Cf eluted with pH 3.7 α-hydroxyisobutyrate
Solution loaded on Dowex -1 Anion Resin
Column stripped with pH 4.2 α-hydroxyisobutyrate
Column washed with HNO_3, then HCl
Eluent dried, picked up in HCl
Pu eluted with HI/HCl
Np eluted with HCl/HF
Activity loaded on sat'd HCl AG MP 50 Cation Column, Am, Cm and Bk eluted
XBL 836-10391

Figure 4.3

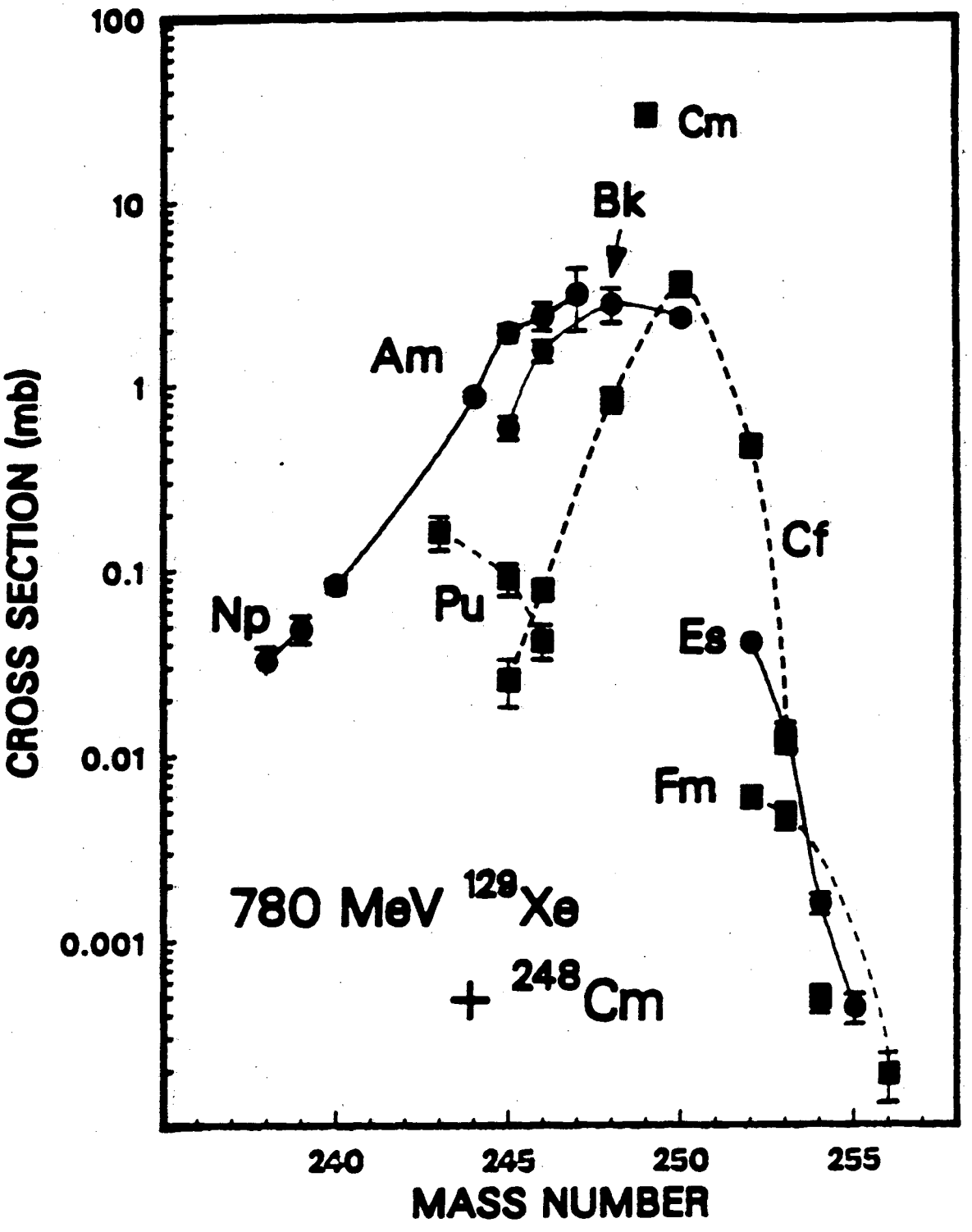

XBL 851-747

Figure 6.1

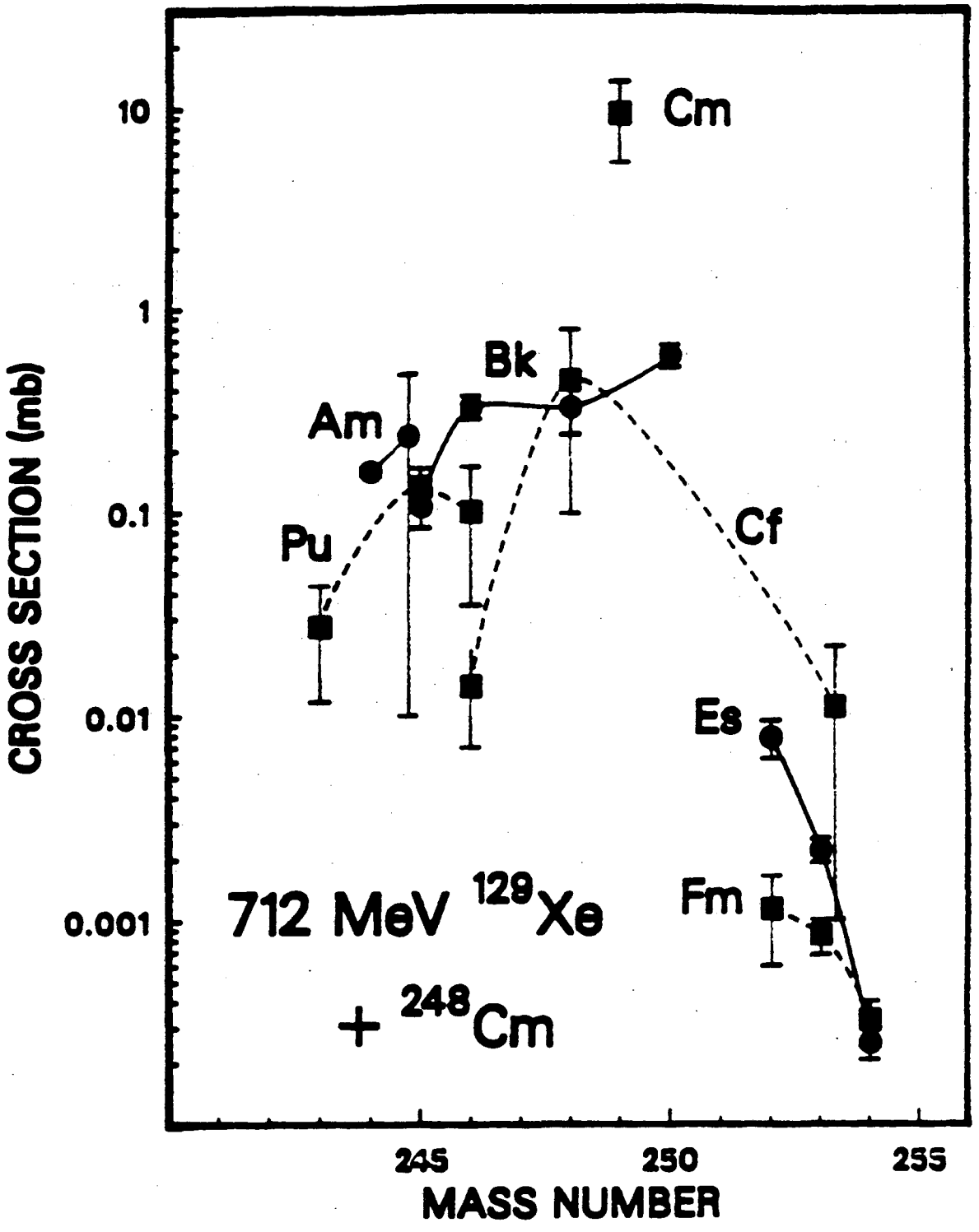

XBL 851-748

Figure 6.2

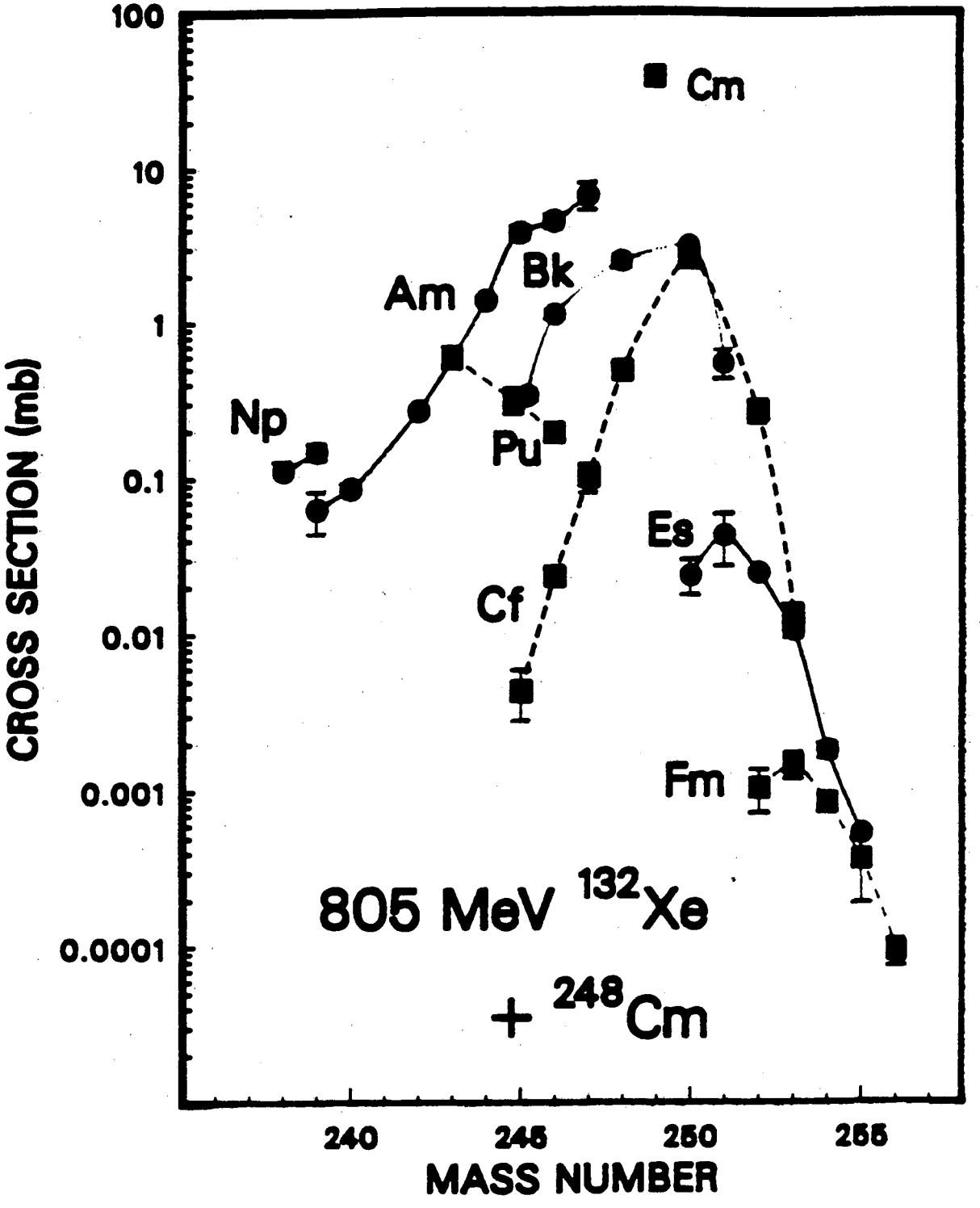

XBL 851-746

Figure 6.3

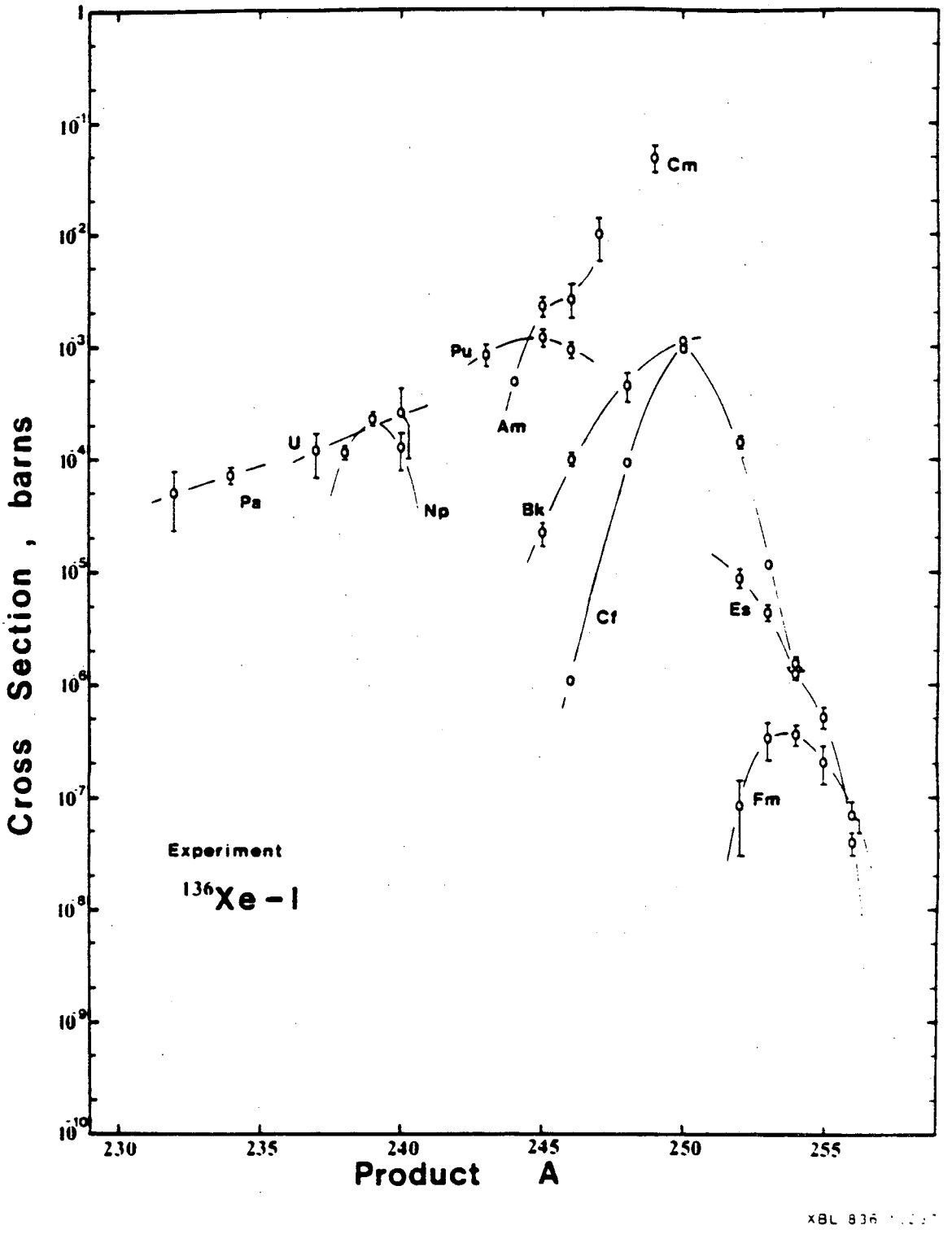
Cross Section , barns
Product A
Experiment
^{136}Xe – I
Cm
Pu
Am
U
Pa
Np
Bk
Cf
Es
Fm
1
10^{-1}
10^{-2}
10^{-3}
10^{-4}
10^{-5}
10^{-6}
10^{-7}
10^{-8}
10^{-9}
10^{-10}
230
235
240
245
250
255
XBL 836

Figure 6.4

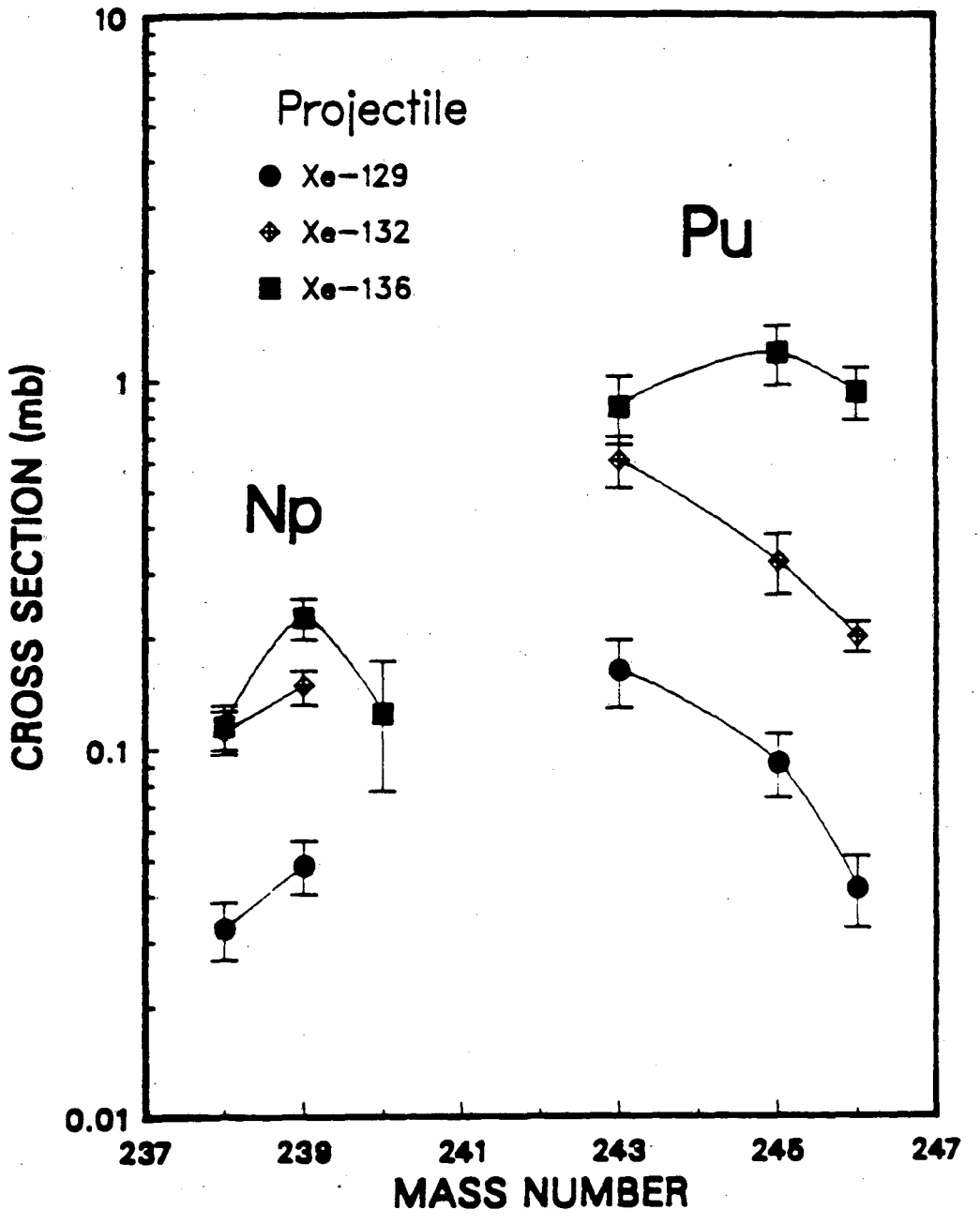
Xe + 248Cm → Np,Pu
Projectile
Xe-129
Xe-132
Xe-136
Np
Pu
CROSS SECTION (mb)
10
1
0.1
0.01
237
239
241
243
245
247
MASS NUMBER
XBL 851-742

Figure 6.5

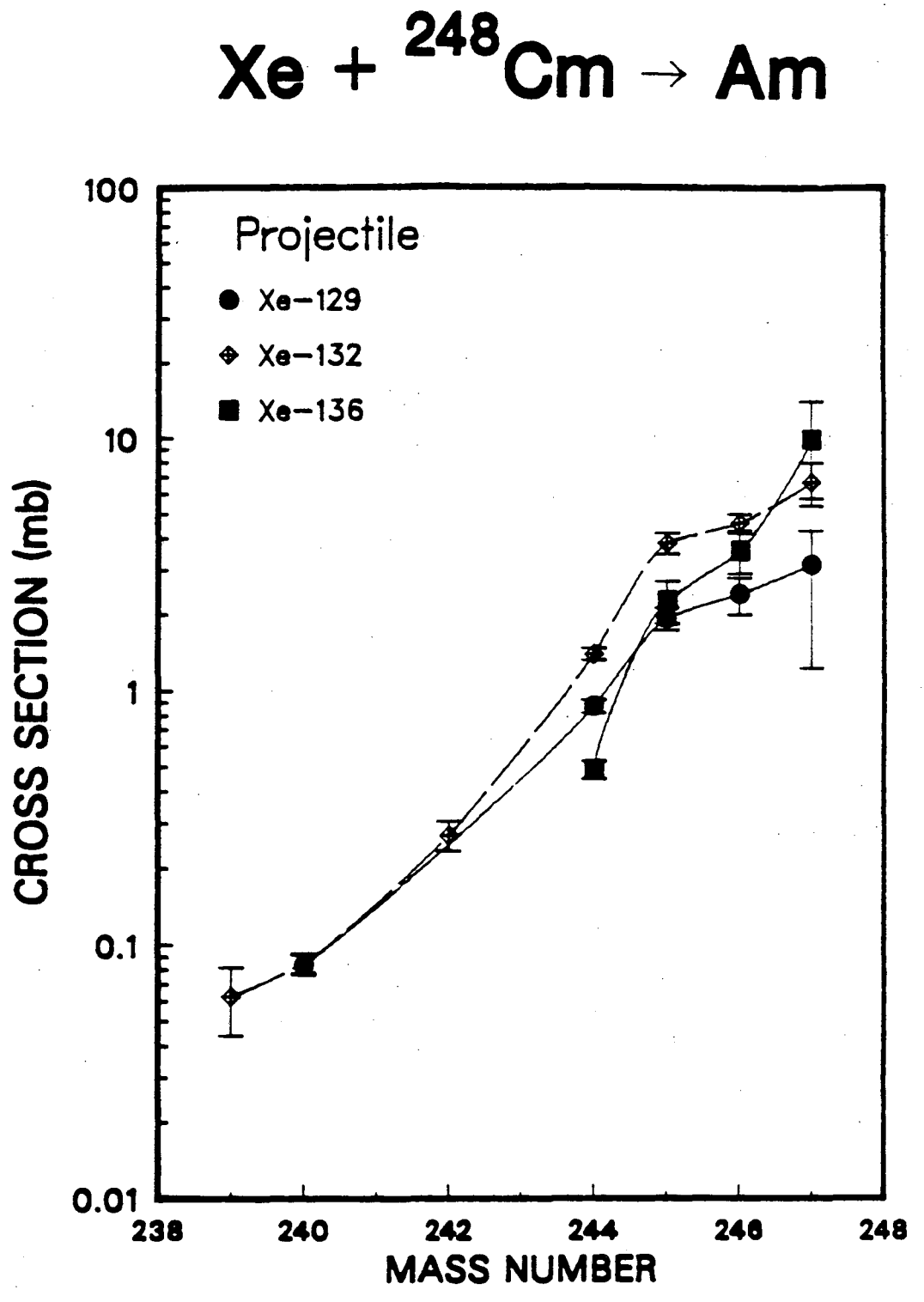
Xe + 248Cm → Am
Projectile
Xe-129
Xe-132
Xe-136
CROSS SECTION (mb)
100
10
1
0.1
0.01
238
240
242
244
246
248
MASS NUMBER
XBL 851-743

Figure 6.6

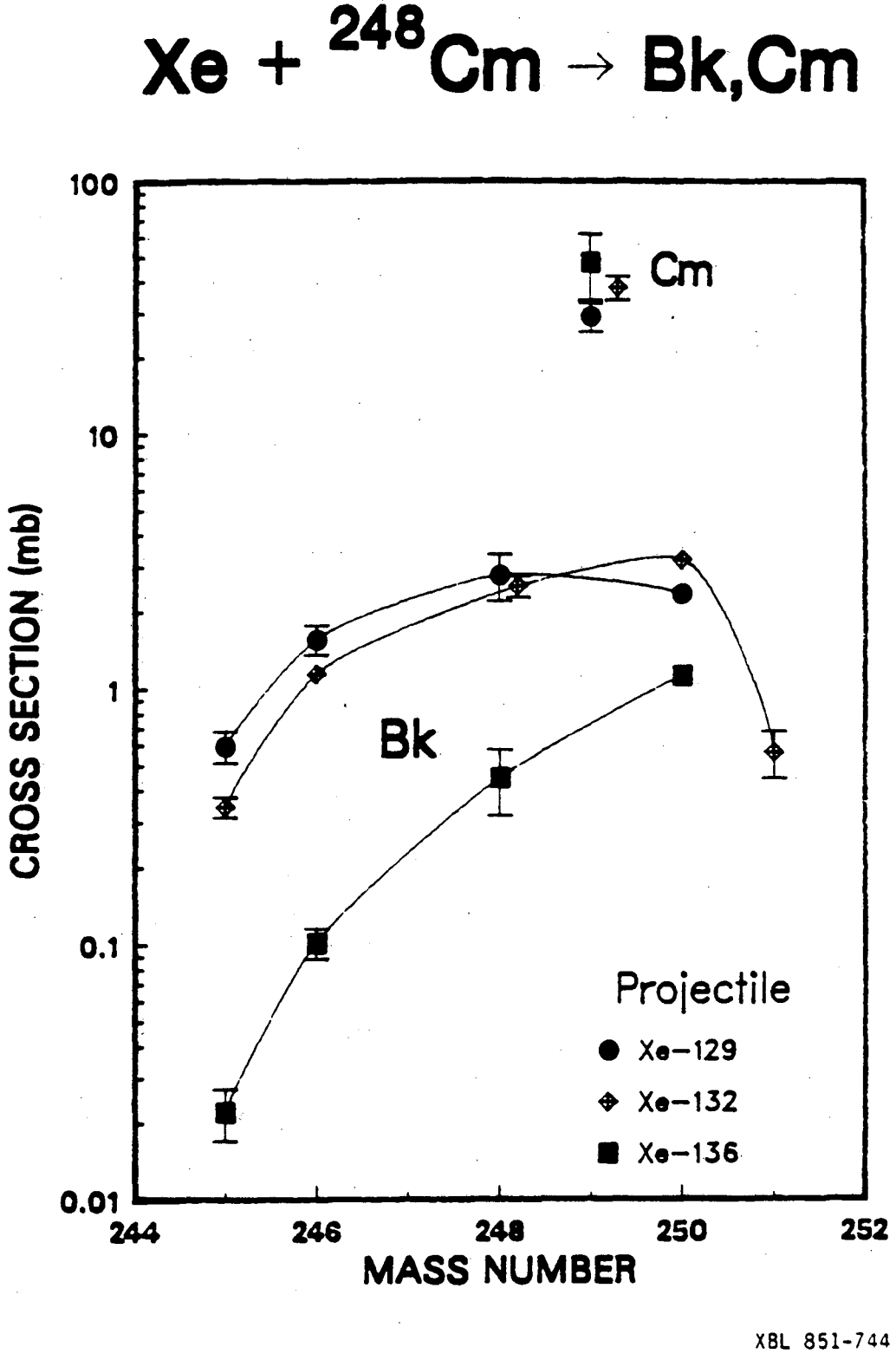
Xe + 248Cm → Bk,Cm
100
10
1
0.1
0.01
CROSS SECTION (mb)
Cm
Bk
Projectile
Xe-129
Xe-132
Xe-136
244
246
248
250
252
MASS NUMBER
XBL 851-744

Figure 6.7

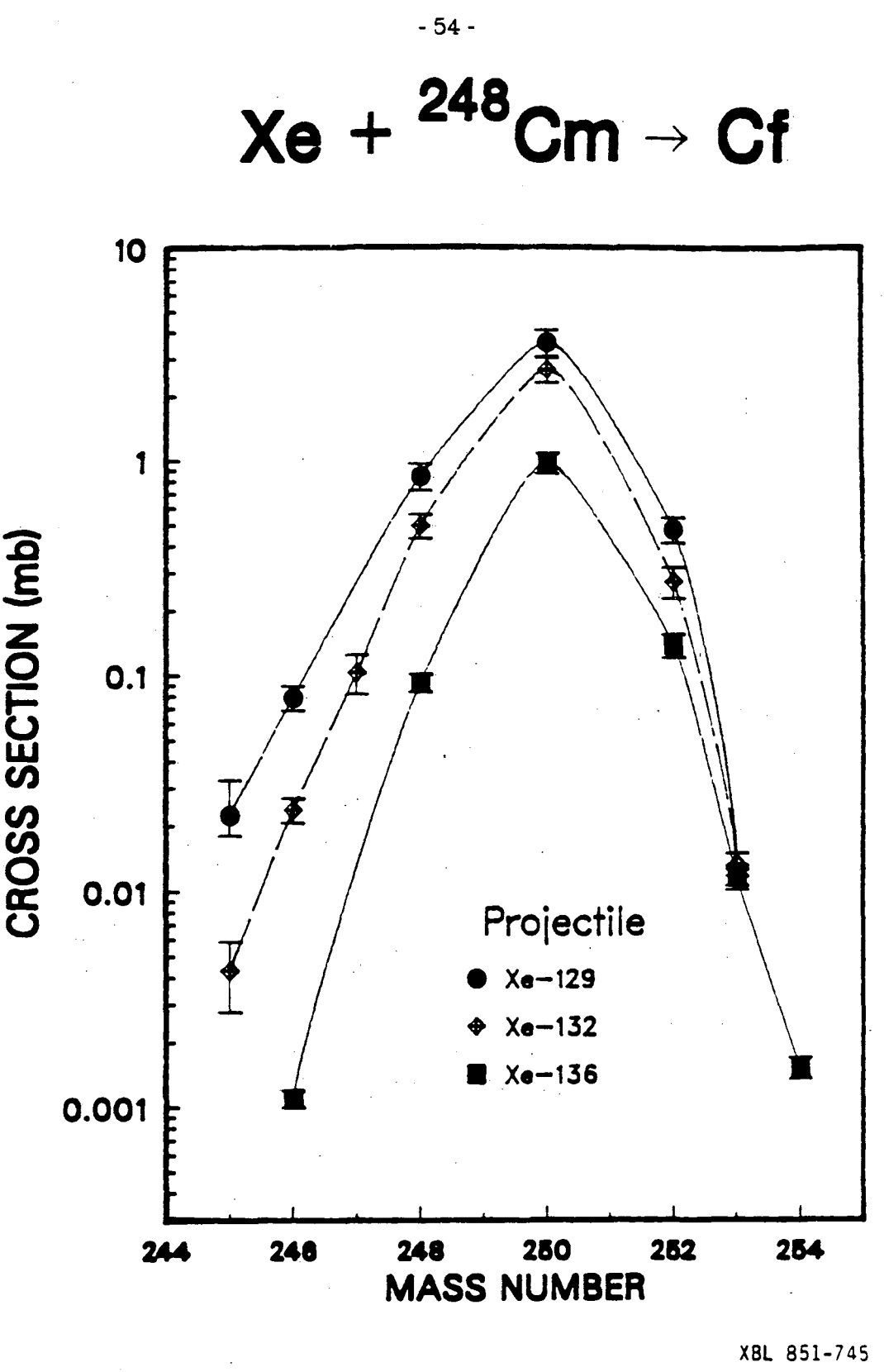
Xe + 248Cm → Cf
10
1
0.1
0.01
0.001
CROSS SECTION (mb)
244
246
248
250
252
254
MASS NUMBER
Projectile
Xe-129
Xe-132
Xe-136
XBL 851-745

Figure 6.8

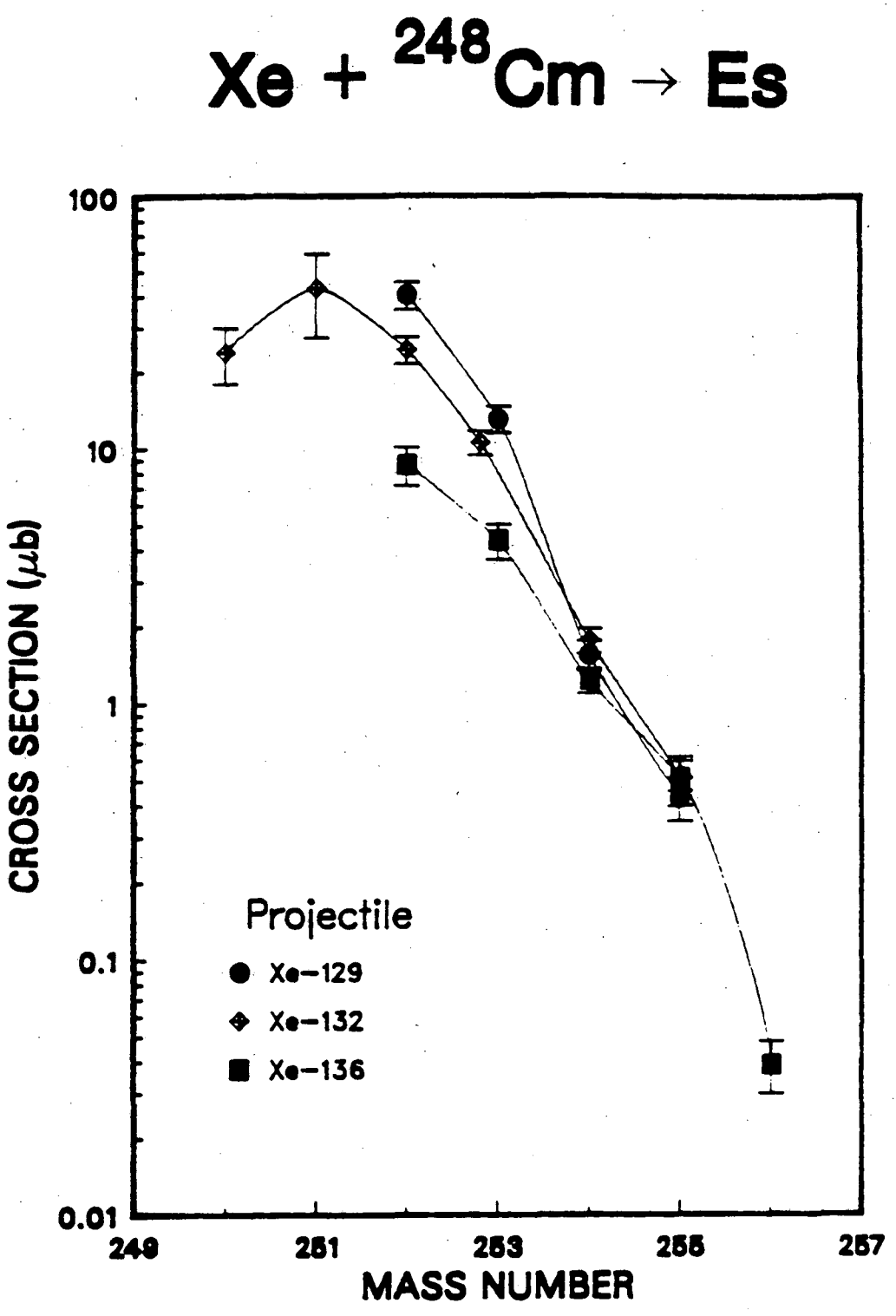
Xe + 248Cm → Es
100
10
1
0.1
0.01
CROSS SECTION (μb)
249
251
253
255
257
MASS NUMBER
Projectile
Xe-129
Xe-132
Xe-136
XBL 851-740

Figure 6.9

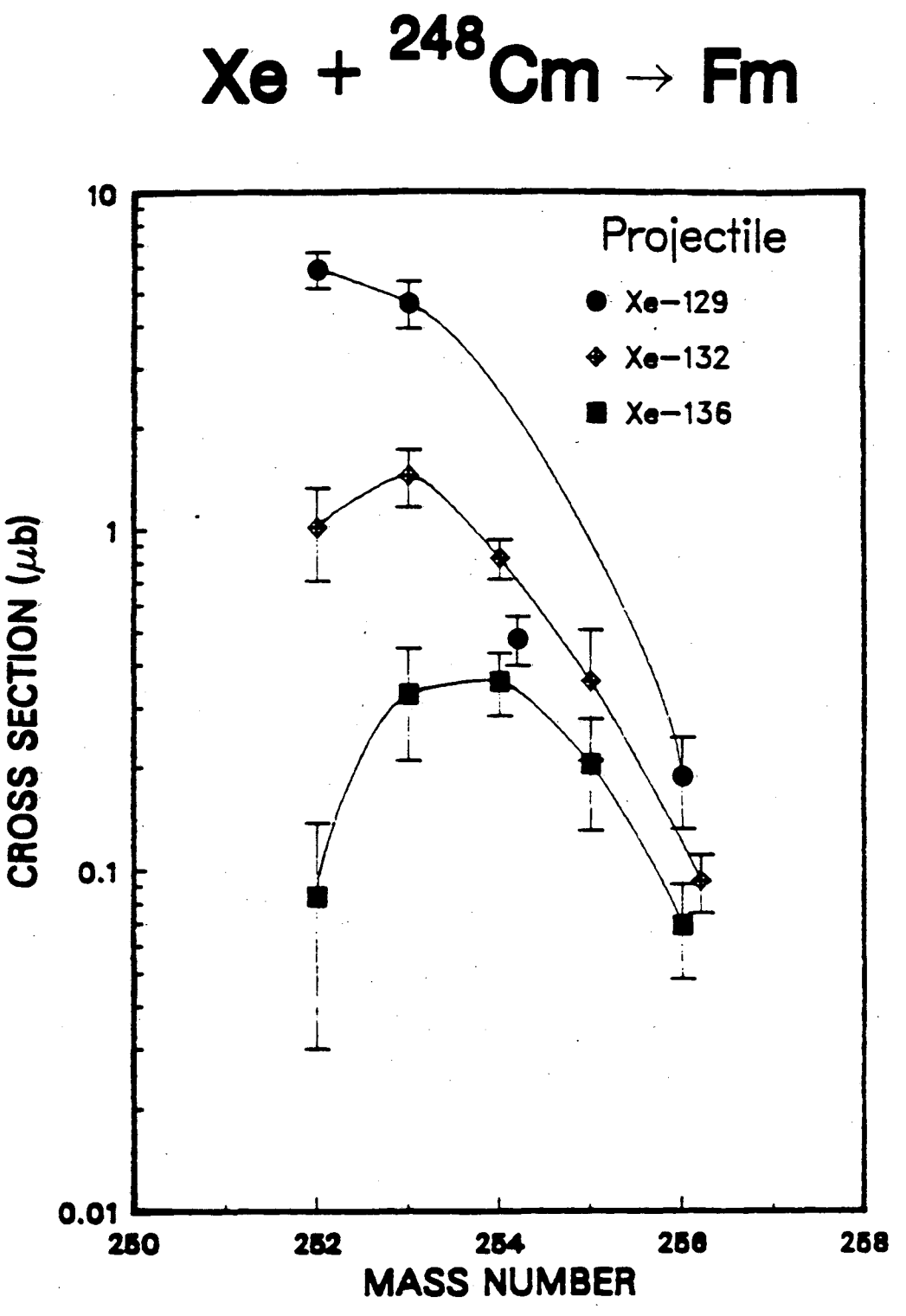
Xe + 248Cm → Fm
Projectile
Xe–129
Xe–132
Xe–136
CROSS SECTION (μb)
10
1
0.1
0.01
250
252
254
256
258
MASS NUMBER
XBL 851-741

Figure 6.10

PROJECTILE Z= 54, A= 132

TARGET Z = 56, A = 248

INITIAL ENERGY = 805.00 MEV (525.37 MEV IN C.M. FRAME)

INITIAL ANG. MOM. = 150.00 HBAR AND IMPACT PARAMETER = 3.208 FM

POTENTIAL ENERGY SURFACE

N \ Z =	88	89	90	91	92	93	94	95	96	97	98	99	100	101	102	103
140								5.80	8.35	13.29	18.81	24.16	32.53	42.53	54.20	65.81
141							.05	1.93	5.42	9.61	14.06	20.67	27.19	37.37	47.80	58.91
142						-3.35	-2.33	-.25	2.60	6.05	10.99	16.20	22.74	31.93	41.75	52.59
143					-4.41	-4.43	-3.72	-2.21	.12	3.47	7.38	12.48	18.22	26.74	36.28	47.24
144				-3.13	-4.35	-4.99	-4.81	-3.71	-1.86	.75	4.42	8.87	13.86	22.10	31.53	42.86
145			.51	-2.11	-4.05	-5.22	-5.46	-5.02	-3.70	-1.44	1.67	5.38	10.06	17.97	27.43	36.40
146		6.48	2.30	-.92	-3.42	-5.12	-6.01	-5.57	-5.10	-3.37	-.97	2.37	6.59	14.28	22.06	31.55
147	14.61	8.88	4.42	.57	-2.68	-4.81	-6.06	-6.56	-6.25	-5.17	-3.17	-.40	3.35	9.94	17.86	26.50
148	17.63	11.57	6.77	1.84	-1.44	-3.56	-5.81	-6.96	-7.20	-6.58	-5.21	-2.97	.05	6.43	13.59	21.51
149	23.66	17.13	10.43	6.09	2.31	-.87	-3.51	-5.07	-5.81	-5.81	-5.01	-3.31	-.67	5.04	11.64	19.60
150	25.69	21.10	15.79	10.76	6.27	2.11	-.78	-2.91	-4.24	-4.77	-4.44	-3.25	-1.22	4.03	10.16	16.87
151	33.86	27.68	21.40	15.63	9.89	5.67	2.15	-.49	-2.26	-3.34	-3.56	-2.92	-1.32	3.17	8.74	14.99
152	41.73	34.22	27.18	19.84	14.29	9.35	5.43	2.55	0.	-1.61	-2.31	-2.11	-1.37	2.90	7.85	13.94
153	49.22	40.53	31.55	25.06	18.69	13.54	9.63	5.57	2.62	.58	-.63	-1.16	-.66	2.95	7.51	12.73
154	56.77	46.18	37.98	30.18	23.82	19.00	13.38	9.10	5.77	3.11	1.50	.39	.29	3.41	7.39	12.31
155	62.09	52.66	43.59	36.22	30.65	23.42	17.86	13.26	9.13	6.61	3.73	2.19	1.64	4.21	7.76	11.95
156	69.18	58.67	50.24	44.17	35.53	28.88	23.04	17.41	14.17	9.36	6.34	4.53	3.20	5.31	8.16	
157	75.82	66.26	59.59	49.32	41.64	34.51	27.96	24.19	17.29	12.73	9.76	6.72	4.95	6.54		
158	84.46	77.27	65.22	56.37	48.52	40.23	36.47	27.51	21.36	17.32	12.41	9.06	7.09			
159	91.28	83.35	73.35	64.33	54.48	50.65	39.54	32.13	27.21	20.27	15.26	12.19				
160	103.87	92.67	82.47	70.95	67.16	53.52	44.55	39.11	30.30	23.56	19.46					
161	114.34	102.59	89.83	86.16	65.77	59.06	52.89	41.96	33.84	28.90						
162	125.51	111.04	107.70	88.37	75.84	68.94	55.54	45.68	40.25							

Figure 8.11

PROJECTILE Z= 54, A= 132

TARGET Z = 96, A = 248

INITIAL ENERGY = 865.00 MEV (525.37 MEV IN C.M. FRAME)

INITIAL ANG. MOM. = 150.00 HBAR AND IMPACT PARAMETER = 3.208 FM

POTENTIAL ENERGY SURFACE

Z = N	88	89	90	91	92	93	94	95	96	97	98	99	100	101	102	103
140								5.80	8.35	13.29	18.81	24.16	32.53	42.53	54.20	65.81
141							.05	1.93	5.42	9.61	14.06	20.67	27.19	37.37	47.80	58.91
142						-3.35	-2.33	-.25	2.60	6.05	10.99	16.20	22.74	31.93	41.75	52.59
143					-4.41	-4.43	-3.72	-2.21	.12	3.47	7.38	12.48	18.22	26.74	36.28	47.24
144				-3.13	-4.35	-4.99	-4.81	-3.71	-1.86	.75	4.42	8.87	13.88	22.10	31.53	42.86
145			.51	-2.11	-4.05	-5.22	-5.46	-5.02	-3.70	-1.44	1.67	5.38	10.06	17.97	27.43	36.40
146		6.48	2.30	-.92	-3.42	-5.12	-6.01	-5.57	-5.10	-3.37	-.97	2.37	6.59	14.28	22.06	31.55
147	14.61	6.88	4.42	.57	-2.68	-4.81	-6.06	-6.56	-6.25	-5.17	-3.17	-.40	3.35	9.94	17.86	26.50
148	17.63	11.57	6.77	1.84	-1.44	-3.56	-5.81	-6.96	-7.20	-6.58	-5.21	-2.97	.05	6.43	13.59	21.51
149	23.66	17.13	10.43	6.09	2.31	-.87	-3.51	-5.07	-5.81	-5.81	-5.01	-3.31	-.67	5.04	11.64	19.60
150	29.69	21.10	15.79	10.76	6.27	2.11	-.78	-2.91	-4.24	-4.77	-4.44	-3.25	-1.22	4.03	10.16	16.87
151	33.86	27.68	21.40	15.63	9.89	5.67	2.15	-.49	-2.26	-3.34	-3.56	-2.92	-1.32	3.17	8.74	14.99
152	41.73	34.22	27.18	19.84	14.29	9.35	5.43	2.55	0.	-1.61	-2.31	-2.11	-1.37	2.90	7.85	13.94
153	49.22	40.53	31.55	25.06	18.69	13.54	9.63	5.57	2.62	.58	-.63	-1.16	-.66	2.55	7.51	12.73
154	56.77	46.18	37.98	30.18	23.82	19.00	13.38	9.10	5.77	3.11	1.50	.39	.29	3.41	7.39	12.31
155	62.09	52.66	43.59	36.22	30.65	23.42	17.86	13.26	9.13	6.61	3.73	2.19	1.64	4.21	7.76	11.95
156	69.18	58.67	50.24	44.17	35.53	28.88	23.04	17.41	14.17	9.36	6.34	4.53	3.20	5.31	8.16	
157	75.82	66.26	59.59	49.22	41.64	34.51	27.96	24.19	17.29	12.73	9.76	6.72	4.95	6.54		
158	84.46	77.27	65.22	56.37	48.52	40.23	36.47	27.51	21.36	17.32	12.41	9.06	7.09			
159	91.28	83.35	73.35	64.33	54.48	50.65	39.54	32.13	27.21	20.27	15.26	12.19				
160	103.87	92.67	82.47	70.95	67.16	53.52	44.55	39.11	30.30	23.56	19.46					
161	114.34	102.99	89.83	86.16	69.77	59.06	52.89	41.96	33.84	28.90						
162	125.91	111.04	107.70	88.37	75.84	68.94	55.54	45.68	40.25							

Figure 8.12

PROJECTILE Z= 54, A= 136

TARGET Z = 96, A = 248

INITIAL ENERGY = 745.00 MEV (481.15 MEV IN C.M. FRAME)

INITIAL ANG. MOM. = 150.00 HBAR AND IMPACT PARAMETER = 3.320 FM

POTENTIAL ENERGY SURFACE

Z = / N	88	89	90	91	92	93	94	95	96	97	98	99	100	101	102	103
140								17.41	21.59	28.11	34.92	41.36	50.83	61.90	74.26	85.36
141							10.04	13.52	18.59	24.20	29.76	37.48	45.11	56.37	67.77	78.94
142						5.10	7.67	11.31	15.61	20.22	26.28	32.61	40.27	50.55	61.45	72.81
143					2.58	4.07	6.28	9.23	12.74	17.21	22.25	28.48	35.36	44.97	55.60	67.51
144				2.45	2.70	3.50	5.05	7.31	10.30	14.05	18.86	24.45	30.61	39.93	50.46	62.90
145			4.79	3.54	2.95	3.06	3.55	5.53	8.00	11.41	15.67	20.53	26.37	35.40	45.97	56.07
146		9.45	6.54	4.57	3.21	2.66	2.92	4.10	6.13	9.02	12.58	17.09	22.47	31.29	40.20	50.82
147	16.34	11.56	8.24	5.54	3.43	2.45	2.36	3.03	4.50	6.76	9.92	13.87	18.85	26.54	35.60	45.38
148	18.60	14.08	10.04	6.26	4.14	2.78	2.10	2.12	3.06	4.87	7.42	10.85	15.06	22.60	30.91	39.99
149	22.10	16.72	11.16	7.98	5.36	3.35	1.88	1.49	1.93	3.11	5.10	7.59	11.83	18.69	26.45	35.57
150	25.57	18.13	13.97	10.10	6.77	3.77	2.06	1.11	.95	1.60	3.13	5.51	8.74	15.14	22.43	30.30
151	27.16	22.12	16.99	12.38	7.80	4.75	2.40	.54	.36	.46	1.43	3.27	6.07	11.71	18.44	25.85
152	32.41	26.05	20.16	13.97	9.58	5.81	3.07	1.36	0.	-.42	.07	1.47	3.41	8.83	14.95	22.20
153	39.20	32.07	24.25	18.52	13.33	9.35	6.63	3.76	1.99	1.16	1.15	1.83	3.55	8.33	14.06	20.45
154	46.16	36.65	29.58	22.96	17.78	14.15	9.72	6.65	4.52	3.07	2.67	2.78	3.91	8.21	13.37	19.48
155	51.20	42.78	34.71	28.36	23.92	17.89	13.54	10.14	7.23	5.93	4.28	3.58	4.66	8.42	13.17	18.56
156	58.10	48.58	41.09	35.94	28.26	22.66	18.03	13.63	11.62	8.04	6.26	5.69	5.62	8.93	12.98	19.12
157	64.56	55.96	50.22	40.84	34.03	28.19	22.27	19.73	14.06	10.75	9.03	7.25	6.74	9.55	13.99	18.63
158	72.86	66.72	55.62	47.63	40.62	33.14	30.26	22.35	17.45	14.66	11.02	8.94	8.24	10.83	14.22	18.40
159	84.97	72.20	63.25	55.25	46.26	43.21	32.50	26.36	22.60	16.53	13.19	11.40	9.66	11.80	14.72	18.43
160	90.67	80.63	71.58	61.21	58.43	45.71	37.49	32.84	24.99	19.52	16.70	12.80	11.37	13.04	15.49	18.72
161	100.16	90.00	78.02	75.52	60.26	50.62	45.38	35.19	27.91	24.14	17.93	15.27	13.35	14.55	16.53	19.29
162	110.70	97.04	94.90	76.77	65.42	55.66	47.34	38.37	33.72	25.04	21.17	18.02	15.62	16.34	17.84********	

Figure 8.13

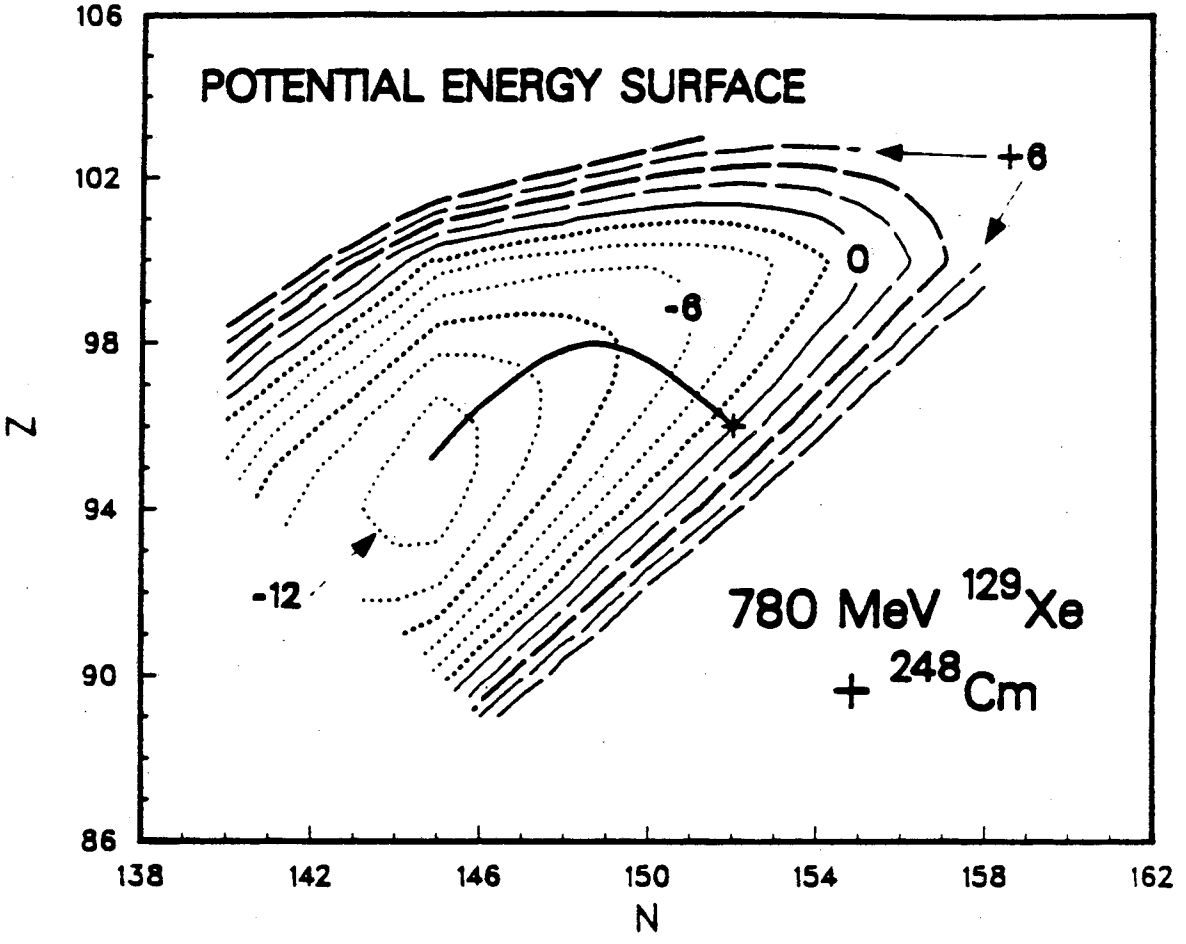
POTENTIAL ENERGY SURFACE
+6
0
-6
-12
780 MeV ^{129}Xe
+ ^{248}Cm
106
102
98
94
90
86
Z
138
142
146
150
154
158
162
N
XBL 851-750

Figure 6.14

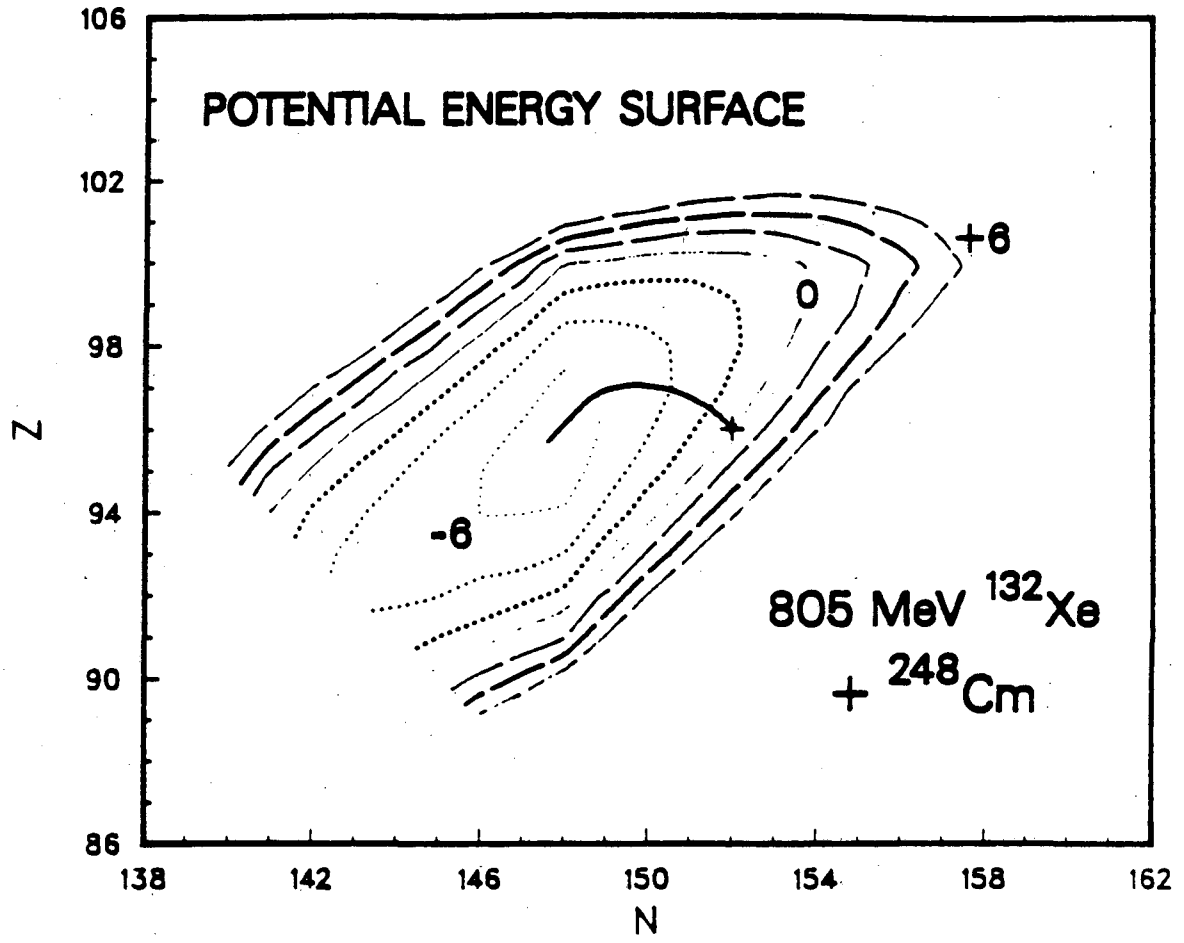
POTENTIAL ENERGY SURFACE
+6
0
-6
805 MeV ^{132}Xe
+ ^{248}Cm
Z
N
106
102
98
94
90
86
138
142
146
150
154
158
162
XBL 851-749

Figure 6.15

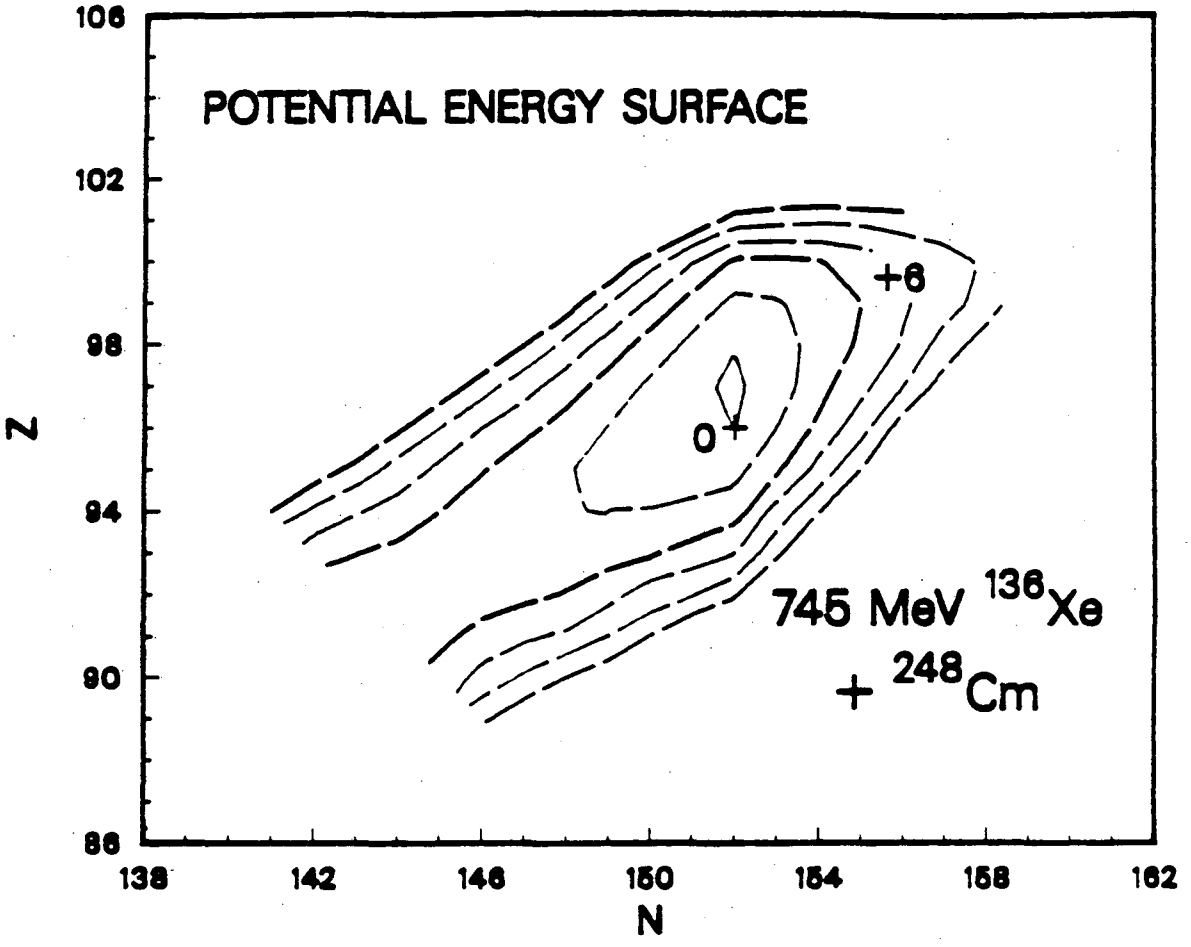

XBL 851-751

Figure 6.16

Table Captions

1) The variation of the calculated PE and excitation energy (E^*) for Fm isotopes from the ^{129}Xe(hi) reaction as a function of three different separation distances R. The choice of R does not significantly affect the PES, but is crucial in the calculation of E^*.

2) For the ^{129}Xe(hi), ^{132}Xe, and ^{136}Xe + ^{248}Cm reactions, the actual peak positions of the production cross sections for Bk, Cf, Es, and Fm are compared with the minimum of the PES for those elements, as well as the mass number, for each element, which has an N/Z ratio equal to the N/Z ratio of the combined target-projectile system. Also shown is the calculated excitation energy for the mass number at the minimum of the PES for each element. These energies have been adjusted to show an excitation energy split between the two products proportional to their mass.

3) For Xe + ^{248}Cm, ^{197}Au reactions, σ_{tot}, σ_{DIR}, and σ_{QE} have been calculated using [Wes83]. For ^{129}Xe + ^{197}Au, the experimentally determined σ_{DIR} and σ_{QE} are shown. For these near barrier reactions, the QE and DIR contributions are of the same magnitude. R_{INT} is Eqn. 6.13 and $l(t_m)$ is the angular momentum of the system needed to keep the centers of the reactants within R_{INT} of each other for time t_m (Eqn. 6.11).

Table 1

	^{129}Xe (780 MeV)	^{132}Xe (805 MeV)	^{136}Xe (745 MeV)
	Mass Number at PES Minimum		
Fm	250	251.5	252
Es	247	248.5	251
Cf	244	246	250
Bk	242	245	249
	Experimental Peak Position Mass Number		
Fm	≤ 252	253	253.5
Es	≤ 252	251	≤ 252
Cf	$248 \leq P \leq 252$	$248 \leq P \leq 252$	$248 \leq P \leq 252$
Bk	248	250	≥ 250
	Peak Mass Number Assuming N/Z of Total System		
Fm	251.3	253.3	256
Es	248.8	250.8	253.4
Cf	246.3	248.3	250.9
Bk	243.8	245.7	248.3
	Calculated Excitation Energy (MeV) at PES Minimum		
Fm	23.6	29.7	< 0
Es	24.2	30.4	< 0
Cf	25.0	31.2	< 0
Bk	26.0	31.9	< 0

Table 2

780 MeV ^{129}Xe + ^{248}Cm → Fm		
	R_{int}	
A	PES (MeV)	E^* (MeV)
248	-5.42	23.02
249	-5.71	23.38
250	-5.83	23.63
251	-5.48	23.57
252	-5.08	23.48
	$R_{1.36}$	
248	-4.88	32.64
249	-5.16	33.02
250	-5.26	33.29
251	-4.89	33.26
252	-4.48	33.18
	$R_{14.5}$	
248	-6.50	3.62
249	-6.82	4.00
250	-6.96	4.27
251	-6.64	4.24
252	-6.28	4.19

$R_{int} = C_T + C_P + 4.49 - (C_T + C_P)/6.35 = 15.42$ fm

$R_{1.36} = 1.36 * (A_1^{1/3} + A_2^{1/3}) + .5 = 15.92$ fm

$R_{14.5} = 14.5$ fm

Table 3

	E_{lab} (MeV)	R_{int} (fm)	$l(t_m)\hbar$	calculated cross sections (mb) σ_r	σ_{DIR}	σ_{QE}
$^{129}Xe + ^{248}Cm$	791 - 769 MeV	15.94	152	707	348	361
^{132}Xe	817 - 793 MeV	15.99	188	906	511	395
^{136}Xe	790 - 699 MeV	16.06	72	376	78	297
$^{129}Xe + ^{197}Au$	≤ 761 MeV	15.34	106	505	221	284
^{132}Xe	≤ 764 MeV	15.39	106	501	218	283
^{136}Xe	≤ 787 MeV	15.46	123	583	286	296

For $^{129}Xe + ^{197}Au$, the experimentally determined cross sections are: σ_{DIR} = 216 mb and σ_{QE} = 190 mb.

References

[Arm82] Armbruster, P., Gesellschaft für Schwerionenforschung preprint GSI-82-5 (1982).

[Bir79] Birkelund, J.R., L.E. Tubbs, J.R. Huizenga, J.N. De, D. Sperber, Physics Reports 56, 109 (1979).

[Blo77] Blocki, J., J. Randrup, W.J. Swiatecki, C.F. Tsang, Annals of Physics 105, 427 (1977).

[Boc74] Bock, R., Nuclear Spectroscopy and Reactions, Cerny,J. ed., Academic Press (New York 1974).

[Bon74] Bondorf, J.P., M.I. Sobel, D. Sperber, Physics Reports 15C, 83 (1974).

[Cho56] Choppin,G.R., R.J. Silva, J.Inorg and Nucl.Chem. 2, 66 (1956).

[Fre79] Freiesleben, H., K.D. Hildenbrand, F. Pühlhofer, W.F.W. Schneider, R. Bock, D.v. Hanach, H.J. Specht, Z. Physik A 292, 171 (1979).

[Fre84] Freiesleben, H., J.V. Kratz, Physics Reports, 106, 1 (1984).

[Gäg83] Gäggeler, H., et. al., Gesellschaft für Schwerionenforschung preprint GSI-83-9 (1983).

[Gob81] Gobbi, A. Nucl. Physics A354, 337 (1981).

[Gro81] Gross, D.H., K.M. Hartmann, Phys. Rev. C 24, 2526 (1981).

[Gro80] Grossmann, S., Z. Physik A 298, 251 (1980).

[Gru76] Grunder, H.A., F.B. Selph, Lawrence Berkeley Laboratory Report LBL-5390 (1976).

[Heu78] Heusch, B., C. Volant, H. Freiesleben, R.P. Chestnut, K.D. Hildenbrand, F. Pühlhofer, W.F.W. Schneider, B. Kohlmeyer, W. Pfeffer, Z.Physik A 288, 391 (1978).

[Hil77] Hildenbrand, K.D., H. Freiesleben, F. Pühlhofer, W.F.W. Schneider, R. Bock, D.v. Harrach, H.J. Specht, Phys. Rev. Lett. 39, 1065 (1977).

[Hub80] Hubert, F., A. Fleury, R. Bimbot, D. Gardes, Annales de Physique 5, 1 (1980).

[Kno79] Knoll,G.F., Radiation Detection and Measurement, Wiley (New York 1979).

[Kra76] Kratz, J.V., J.O. Liljenzin, A.E. Norris, G.T. Seaborg, Phys. Rev. C 13, 2347 (1976).

[Kra77] Kratz, J.V., H. Ahrens, W. Bögel, W. Brüchle, G. Franz, M. Schädel, I. Warnecke, G. Wirth, G. Klein, M. Weis, Phys. Rev. Lett. 39, 984 (1977).

[Kra79] Kratz, J.V., W. Brüchle, G. Franz, M. Schädel, I. Warnecke, G. Wirth, Nucl. Phys. A332, 477 (1979).

[Kra81] Kratz, J.V., J. Poitou, W. Brüchle, H. Gäggeler, M. Schädel, G. Wirth, R. Lucas, Nucl. Phys. A357, 437 (1981).

[Mai71] Main, R., Nucl. Inst. and Methods 97, 51 (1971).

[Mer83] Merchant, A.C., A.K. Dhar, J. Phys G:Nucl Phys. 9, 21 (1983).

[Mey67] Meyerhof, W.E., Elements of Nuclear Physics, McGraw-Hill (New York 1967).

[Moo63] Moore, F.L., Analytical Chem. 35, 715 (1963).

[Moo80] Moody, K.J., Welch, R.B., computer code RANGY, private communication (1980).

[Moo83] Moody, K.J., Lawrence Berkeley Laboratory Report LBL-16249, (Ph.D. Thesis) (1983).

[Mor83] Moretto, L.G., Nucl. Phys. A409, 115 (1983).

[Mul75] Mullen, G., D.C. Aumann, Nucl. Inst. and Meth. 128, 425 (1975).

[Mye77] Myers, W.D., Droplet Model of Atomic Nuclei, IFI/Plenum (New York 1977).

[Nör80] Nörenberg, W., Heavy Ion Collisions, Vol 2, Bock, R. ed., North Holland Publishing (Amsterdam 1980).

[Ran78] Randrup, J., Annals of Physics 112, 256-65 (1978).

[Rus77] Russo, P., R.P. Schmitt, G.J. Wozniak, B. Cauvin, P. Glässel, R.C. Jared, L.G. Morreto, Phys. Lett. 67B, 155 (1977).

[Sch77] Schröder, W.U., J. Huizenga, Ann. Rev. of Nucl. Sci. 127, 465 (1977).

[Sch81] Schüll, D., W.C. Shen, H. Freiesleben, R. Bock, F. Busch, D. Bangert, W. Pfeffer, F. Pühlhofer, Physics Lett. 102B, 116 (1981).

[Sch82] Schädel, M., W. Brüchle, H. Gäggelesr, J.V. Kratz, K. Sümmerer, G. Wirth, G. Herrmann, R. Stakemann, G. Tittel, N. Trautmann, J.M. Nitschke, E.K. Hulet, R.W. Lougheed, R.L. Hahn, R.L.Ferguson, Phys. Rev. Lett. 48, 852 (1982).

[SHL76] SuperHILAC User's Handbook, Lawrence Berkeley Laboratory (1976).

[Sta81] Staples, J.W., H.D. Lancaster, R.B. Yourd, Lawrence Berkeley Laboratory Report LBL-11693 (1981).

[Tan81] Tanabe, T. R. Bock, M. Dakowski, A. Gobbi, H. Sann, H. Stelzer, Nucl. Phys. A342, 194 (1980).

[Tho54] Thompson, S.G., B.G. Harvey, G.R. Choppin, G.T.Seaborg, J.Am.Chem.Soc. 76, 6229 (1954).

[TOI78] Table of Isotopes, 7th ed., Ed: C.M. Lederer, V. Shirley (New York 1978).

[Vol78] Volkov, V.V., Physics Reports 44, 93 (1978).

[Wes83] Westmeier, W., U. Brosa, Z.Phys A 312, 281 (1983).

[Wil73] Wilczynski, J., Nucl. Phys. A216, 386 (1973).

[Wu 81] Wu, E.C., K.D. Hildenbrand, H. Freiesleben, A. Gobbi, A. Olmi, H. Sann, U. Lynen, Phys. Rev. Lett. 47, 1874 (1981).

TECHNICAL INFORMATION DEPARTMENT
LAWRENCE BERKELEY LABORATORY
UNIVERSITY OF CALIFORNIA
BERKELEY, CALIFORNIA 94720